

## RESEARCH ARTICLE

10.1029/2018JB016574

## Key Points:

- Multicomponent OBS data show variations in gas hydrate distribution in contourite drift sediments of Vestnesa Ridge
- *P* and *S* wave velocities and 1-D FWI models provide better constraints on gas hydrate and free gas saturation estimates
- The distribution of gas hydrates and free gas in Vestnesa Ridge is controlled by the presence of shallow faults

## Correspondence to:

S. Singhroha,  
Sunny.Singhroha@uit.no

## Citation:

Singhroha, S., Chand, S., & Bünz, S. (2019). Constraints on gas hydrate distribution and morphology in Vestnesa Ridge, western Svalbard margin, using multicomponent ocean-bottom seismic data. *Journal of Geophysical Research: Solid Earth*, 124, 4343–4364. <https://doi.org/10.1029/2018JB016574>




Received 17 AUG 2018

Accepted 19 APR 2019

Accepted article online 26 APR 2019

Published online 22 MAY 2019

## Constraints on Gas Hydrate Distribution and Morphology in Vestnesa Ridge, Western Svalbard Margin, Using Multicomponent Ocean-Bottom Seismic Data

Sunny Singhroha<sup>1</sup> , Shyam Chand<sup>2,1</sup> , and Stefan Bünz<sup>1</sup> 

<sup>1</sup>CAGE—Centre for Arctic Gas Hydrate, Environment and Climate, Department of Geosciences, UiT, The Arctic University of Norway, Tromsø, Norway, <sup>2</sup>Geological Survey of Norway (NGU), Trondheim, Norway

**Abstract** Gas hydrates occur within sediments on the western Svalbard continental margin and the Vestnesa Ridge, a large sediment drift that extends in a west-northwest direction from the margin toward the mid-ocean ridge. We acquired multicomponent ocean-bottom seismic (OBS) data at 10 locations on the crest area of the eastern segment of the Vestnesa Ridge, an area with active gas seepage. *P* and *S* wave velocities are estimated using traveltimes inversion, and self-consistent approximation/differential effective medium rock physics modeling is used to estimate gas hydrate and free gas saturation at OBS stations. We apply 1-D full waveform inversion at a selected OBS station to study detailed variations of *P* wave velocity near the bottom simulating reflection (BSR). High interval *P* wave velocity ( $V_p \approx 1.73\text{--}1.82$  km/s) and *S* wave velocity ( $>0.35$  km/s) are observed in a layer above the BSR and low interval *P* wave velocity ( $V_p \approx 1.28\text{--}1.53$  km/s) in a layer below the BSR. We estimate 10–18% gas hydrate and 1.5–4.1% free gas saturation at different OBS stations in a layer above and below the BSR, respectively. We find significant variation in gas hydrate and free gas saturation across faults suggesting a structural control on the distribution of gas hydrate and free gas in the Vestnesa Ridge. Differences in gas hydrate saturation derived from *P* wave velocities and earlier estimates obtained from electromagnetic surveys indicate the presence of gas hydrates in faults and fractures. Moreover, beneath some OBS sites, the combined study of *P* and *S* waves, resistivity and seismic quality factor (*Q*), suggests the coexistence of free gas and gas hydrates.

### 1. Introduction

Gas hydrate is an ice-like crystalline solid formed under high-pressure and low-temperature conditions (Brooks et al., 1986; Sloan, 1998). Gas hydrates are widely present in continental slope and permafrost environments where temperature and pressure conditions are suitable (Sloan, 1998). The presence of gas hydrate in the sediments is often detected by identifying a bottom simulating reflection (BSR) in seismic data (Hyndman & Spence, 1992; Singh et al., 1993). A BSR is a strong seismic reflection at the base of the gas hydrate stability zone (GHSZ), which, due to its dependence on pressure and temperature, often parallels the seafloor (Shipley et al., 1979). Free gas is frequently trapped below the GHSZ due to reduced permeability in gas hydrate-saturated sediments within the GHSZ. This sudden change in the pore fluid at the base of the GHSZ creates a strong impedance contrast resulting in a sharp, polarity-reversed reflection (BSR) in seismic data. A BSR only provides evidence for the presence of gas hydrates but does not allow for estimation of the amount of gas hydrates trapped in sediments. Gas hydrates fill pore space by forming a sediment-hydrate microstructure strengthening the matrix of unconsolidated sediments that in turn increases the bulk modulus, thereby resulting in higher *P* wave seismic velocities compared to sediments not saturated with gas hydrates (Bünz et al., 2005; Chand et al., 2004; Helgerud et al., 1999; Jaiswal et al., 2012; Lee et al., 1996; Lee & Collett, 2009; Lu & McMechan, 2002; Stoll et al., 1971; Yuan et al., 1996). Hence, high *P* wave seismic velocities are observed above the BSR, whereas the presence of free gas in sediments below the BSR reduces the *P* wave velocity. *S* wave velocities may provide further insights about the distribution of hydrates within the pore space of sediments because it depends on the microstructure of sediment-hydrate composite of gas hydrate bearing sediments. The presence of hydrate increases the shear wave velocity when hydrates form as a part of the frame affecting the shear modulus rather than form as pore filling material with no connection to the sediment frame (Bünz et al., 2005; Chand et al., 2004; Kumar et al., 2007; Westbrook et al., 2008). The presence of free gas does not alter the shear strength of sediments overly and thus has little effect on the shear velocity (*V<sub>s</sub>*) of the sediments (Dash & Spence, 2011). Thus, saturation of gas hydrates and free gas

and their distribution patterns in the host sediments can be estimated by performing velocity analysis of both *P* and *S* waves from seismic data (Bünz et al., 2005; Kumar et al., 2007; Song et al., 2018; Westbrook et al., 2008).

In the present study, seismic velocity analysis is performed using multicomponent, wide-angle ocean-bottom seismic (OBS) data acquired at 10 different locations along the eastern segment of the Vestnesa Ridge, offshore western Svalbard. The widespread presence of a BSR provides evidence for the occurrence of gas hydrate in the Vestnesa Ridge sediments (Bünz et al., 2012; Hustoft et al., 2009; Petersen et al., 2010). Gas hydrates have been directly observed and sampled in several of the pockmarks that occur along the crest of the ridge (Panieri et al., 2017). The BSR is most pronounced at the crest of the ridge where topographically controlled fluid migration leads to the accumulation of free gas beneath the BSR (Bünz et al., 2012; Petersen et al., 2010). Here we focus on the crest area of the eastern segment of the Vestnesa Ridge that is characterized by many active seepages of gas from pockmarks at the seafloor (Panieri et al., 2017; Smith et al., 2014). Different structural features like faults and fractures potentially play an important role in active seepage of methane gas in this area (Plaza-Faverola et al., 2015; Singhroha et al., 2016). It is important to study the overall distribution of hydrocarbons (mainly methane) in the system to better understand fluid flow processes. We derive *P* wave and *S* wave seismic velocities from the multicomponent OBS data using traveltime inversion (Zelt & Smith, 1992). At station OBS5, the *P* wave velocity model is further improved using a full-waveform inversion approach (Singh et al., 1993). We use the self-consistent approximation/differential effective medium (SCA/DEM) approach (Chand et al., 2006; Jakobsen et al., 2000) to calculate gas hydrate saturation from the available velocity models at all 10 locations along the ridge. We use this detailed information to study the impact of different structural and stratigraphic factors on the distribution of gas hydrates and free gas in this active fluid flow system in order to better understand fluid flow processes in the Vestnesa Ridge gas hydrate system.

## 2. Study Area

The Vestnesa Ridge is an approximately 100-km-long sediment drift (Figure 1) with a post late Miocene depocenter filled up with mostly contourite deposits (Eiken & Hinz, 1993; Howe et al., 2008). It is located on the western Svalbard continental margin, quite close to a mid-ocean spreading ridge and thus is atop a hot (heat flux  $>115$  mW/m<sup>2</sup>) and young oceanic crust ( $<20$  Ma; Ritzmann et al., 2004; Engen et al., 2008). Sediment thickness in this basin increases from west to east with sediments primarily consisting of glacial debris flows, glacimarine, and hemipelagic sediments (Ottesen et al., 2005; Vogt et al., 1994). The stratigraphy in the Vestnesa Ridge is divided into three seismostratigraphic units; YP-1 (oldest), YP-2, and YP-3 (youngest) sequences (Eiken & Hinz, 1993). Ocean-bottom currents have mainly controlled deposition within the younger sequences (YP-2 and YP-3). The YP-2/YP-3 boundary observed in the seismic data is an unconformity that indicates the onset of Plio-Pleistocene glaciations (Eiken & Hinz, 1993; Knies et al., 2009). The YP-2 sequence is mainly characterized by contourites, and YP-1 has sediments with subparallel reflection patterns that have been deposited during synrift and postrift phases of the tectonic activity in the region (Eiken & Hinz, 1993; Hustoft et al., 2009).

Shallow sediments on Vestnesa Ridge are saturated with hydrocarbon gases, mainly methane, locked in the form of gas hydrates with a 30–100 m-thick free gas layer beneath (Bünz et al., 2012; Goswami et al., 2015; Hustoft et al., 2009). Fluids coming from depths feed into the gas hydrate system on Vestnesa Ridge (Knies et al., 2018), and sediments close to the ridge crest show elevated concentrations of gas hydrates compared to surrounding sediments (Goswami et al., 2015; Hustoft et al., 2009; Singhroha et al., 2016). The presence of gas hydrates near the base of the GHSZ and free gas underneath creates a strong BSR along the ridge (Figure 2; Petersen et al., 2010; Bünz et al., 2012). A recent study by Goswami et al. (2015) has predicted that up to 25% gas hydrate saturation might be present in GHSZ away from focused fluid flow features of Vestnesa Ridge.

The crest of Vestnesa Ridge also shows numerous pockmarks with active seepage of gas (Bünz et al., 2012; Smith et al., 2014). Fluid leakage structures, so-called gas chimneys, exist beneath the pockmarks and provide a pathway for fluids from the free gas zone beneath the BSR to the seafloor (Bünz et al., 2012). Up to 73% gas hydrate saturation might be present within these focused fluid flow features (Goswami et al., 2015).

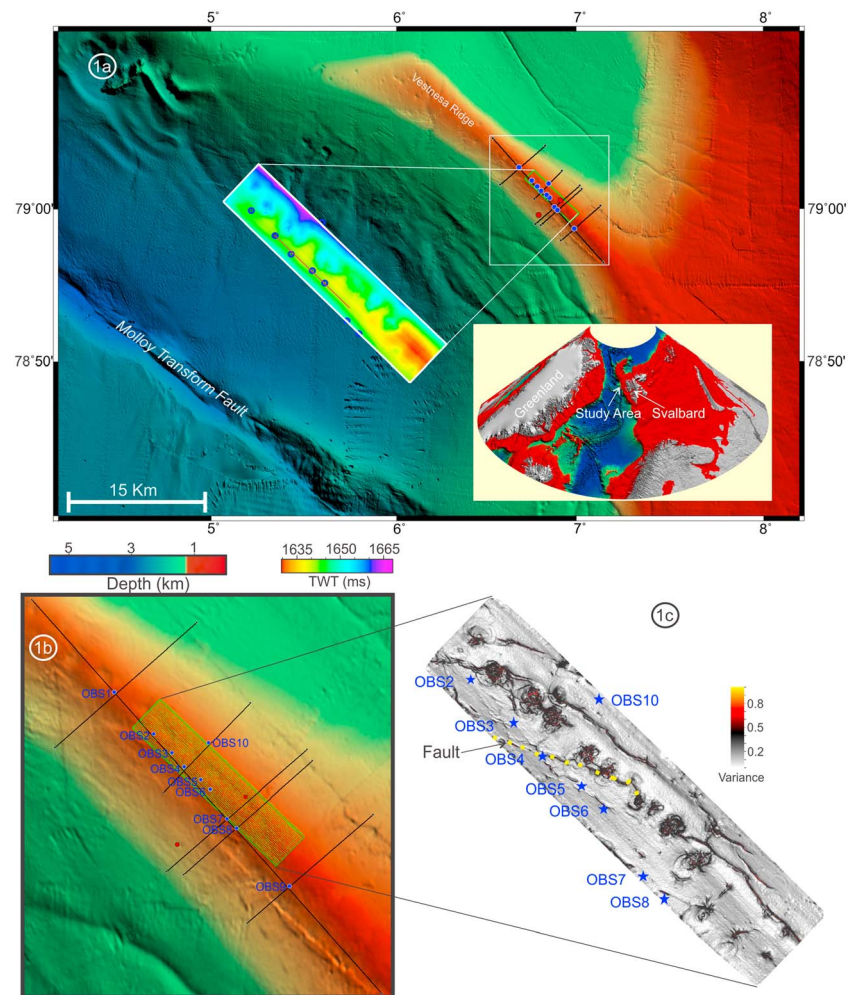


**Figure 1.** (a) Bathymetry map of the study area. Inset figures show the location of the study area and two-way traveltime plot for the seafloor. (b) Location of different OBS stations. Black lines are shot lines used to record OBS data. Green lines show shot lines from 3-D seismic cube. Red dots show the location of OBS stations from Goswami et al. (2015). (c) Location of different OBS stations plotted on variance map illustrating faults (modified from Plaza-Faverola et al., 2015).

### 3. OBS Data Acquisition and Processing

We acquired multicomponent OBS data at 10 different stations near the crest of the Vestnesa Ridge (Figures 1 and 2a). The OBS data used in this study have been acquired in multiple years (Table 1). Nine OBS stations are located on the southwestern flank of the ridge, and one OBS station is located on the northeastern flank of the ridge (Figure 1). In the present study, we have chosen the location of OBS stations such that they will give a comprehensive overview about the variation of gas hydrate saturation along the ridge and potential impact of subsurface structures on the fluid flow system and gas hydrate saturation.

Earlier studies in the region suggest that faults play a significant role in the distribution of gas hydrates (Plaza-Faverola et al., 2015; Singhroha et al., 2016). Significant changes observed in the seismic  $Q$  anomalies across faults suggest substantial changes in hydrate saturation across the fault (Figure 11 in Singhroha et al., 2016). Stations OBS3, OBS4, OBS5, and OBS6 are selected to see the potential difference in seismic velocities across the fault (shown in yellow in Figure 1c) that demarcate seismic  $Q$  anomalies (Singhroha et al., 2016). Locations of OBS1, OBS9, and OBS10 help us to get a regional perspective. Station OBS10, which lies on the northeastern flank of the ridge, is used to see the potential changes in seismic velocities across the ridge. This information can be combined with  $P$  wave velocity analysis from one OBS station (Goswami et al., 2015) that lies at deeper depth on the southwestern flank of the Vestnesa Ridge (Figure 1) to get a regional overview about changes in the seismic velocity across the ridge. Earlier studies have predicted differences in the



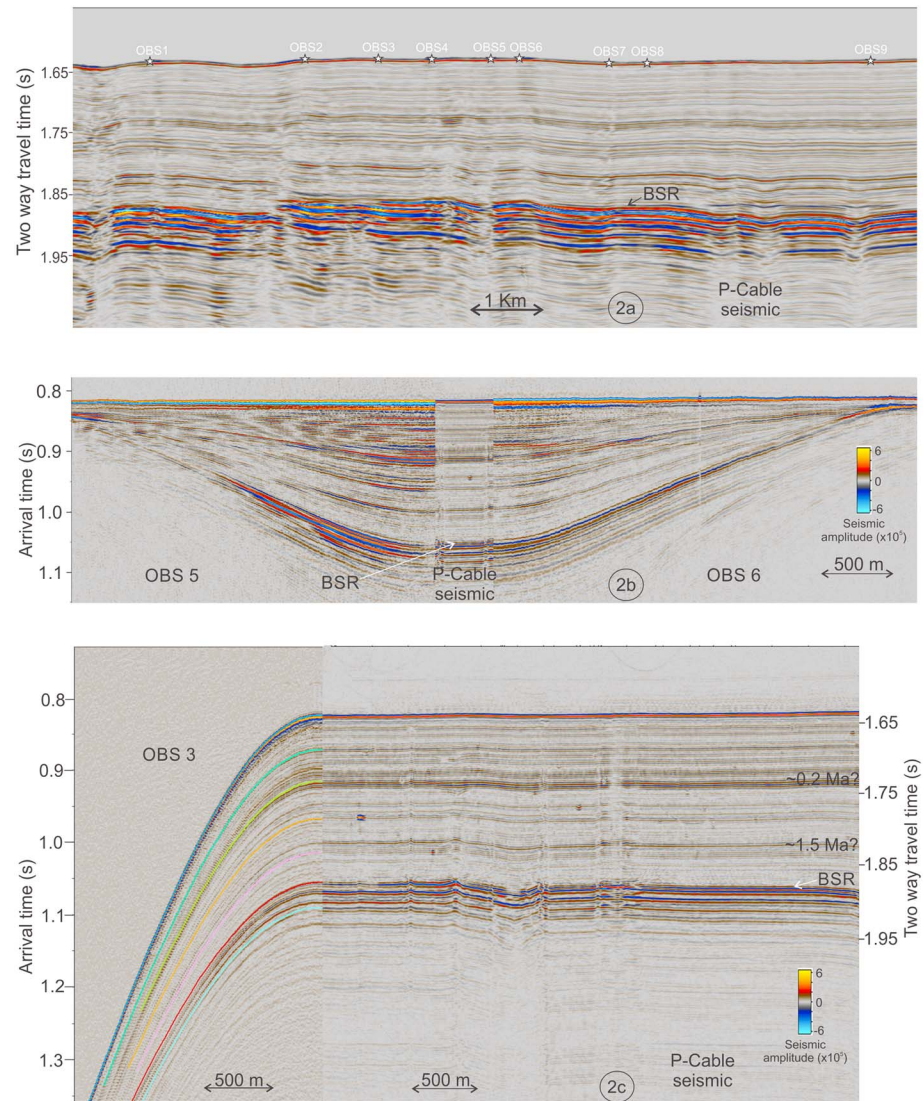


**Figure 2.** (a) Two-dimensional P-Cable seismic data profile passing through nine OBS stations. (b) Offset-corrected OBS5 and OBS6 data placed along with P-Cable data. (c) OBS3 data along with picked arrivals placed along with P-Cable seismic data.

**Table 1**  
*Acquisition Details for OBS Data Set*

OBS station number	Year of data acquisition	Sampling rate (ms)	Shot lines	Acquisition gun
OBS1	2012	0.5	Inline and crossline	GI gun
OBS2	2016	1.0	3-D seismic	GI gun
OBS3	2015	1.0	3-D seismic	Mini GI gun
OBS4	2016	0.4	3-D seismic	GI gun
OBS5	2015	0.4	3-D seismic	Mini GI gun
OBS6	2015	1.0	3-D seismic	Mini GI gun
OBS7	2012	1.0	Inline and crossline	GI gun
OBS8	2012	0.4	Inline and crossline	GI gun
OBS9	2012	0.4	Inline and crossline	GI gun
OBS10	2017	0.4	Inline and crossline along with 3-D seismic	Mini GI gun

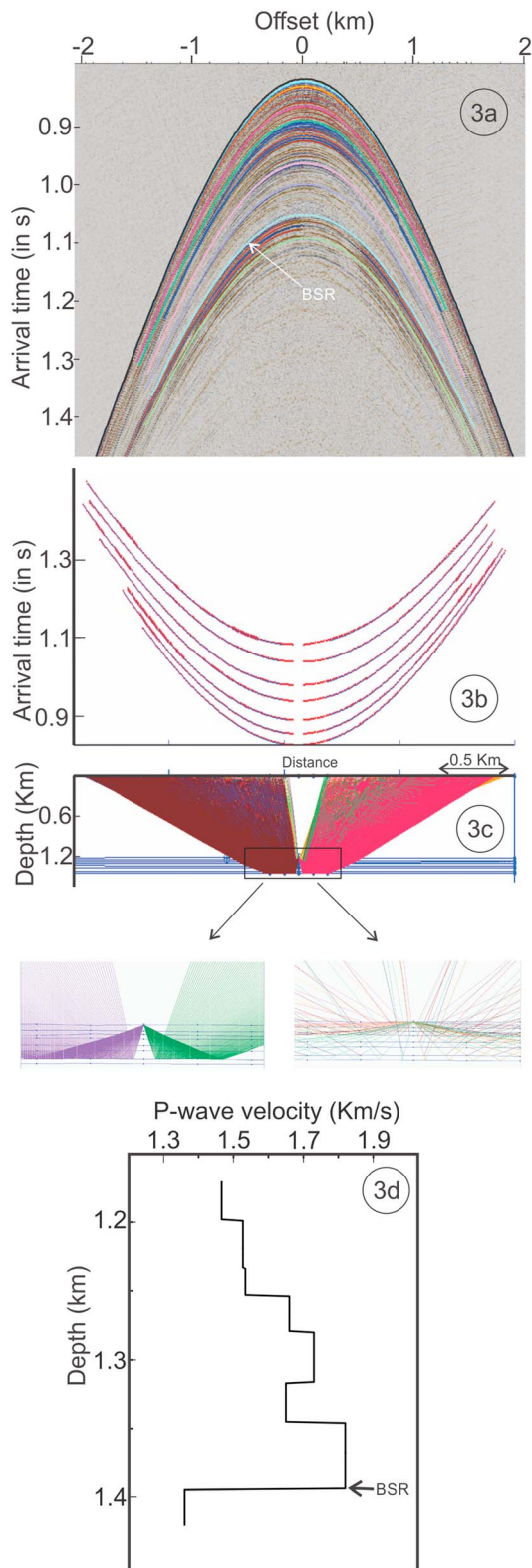


**Figure 3.** (a) *P* wave data recorded by hydrophone at site OBS5. Different picked reflection arrivals are shown in different colors. (b) Picked reflection arrivals and traveltimes corresponding to best fit seismic velocity model. (c) Raypaths corresponding to best fit velocity model. (d) Best fit inverted *P* wave velocity model

distribution of gas across the ridge due to the upward migration of fluids along the slope toward the ridge (Bünz et al., 2012; Hustoft et al., 2009; Singhroha et al., 2016).

Multicomponent OBS records the pressure wavefield using a hydrophone and ground acceleration using a three-component seismometer. Vertical components are used to study *P* waves, and horizontal components are used to study *S* waves. We used a Mini GI air gun (Sercel; 1515 in<sup>3</sup>) or a GI air gun (Sercel; 4545 in<sup>3</sup>) as the active source to acquire high-resolution OBS data, where the two air guns generate seismic energy with frequencies from 20 to 250 Hz (Petersen et al., 2010). The P-cable system (Petersen et al., 2010; Planke et al., 2009) on board *R/V Helmer Hanssen* is used to acquire high-resolution 2-D and 3-D seismic data (Plaza-Faverola et al., 2015) that is integrated with the OBS analysis (Figure 2). The air gun is fired at an interval of 6 s with a firing pressure of 170 bar. Different OBS recorders have different sampling intervals ranging from 0.4 to 1.0 ms (Table 1). We obtain good quality data from the hydrophone component at all OBS stations, which is used for *P* wave velocity analysis. We also obtain good quality records from the three-component seismometer at sites OBS1, OBS2, OBS3, OBS5, and OBS7; however, at other sites, seismometer records are poor quality, probably due to poor coupling between the seismometer and the seafloor.

Processing of OBS data involves some basic steps. The location of an OBS on the seafloor is normally displaced from the location where it was deployed into the water column due to the effect of oceanic currents on the downward path of the OBS. Knowledge of the precise seafloor location of an OBS is prerequisite to an accurate velocity model since velocity analysis is very sensitive to the error in the OBS location. Direct arrivals from inline and crossline directions (plotted in black in Figure 1b) are used to estimate the seafloor location of OBS and seismic velocity in the water column at sites OBS1, OBS7, OBS8, and OBS9. OBS data from sites OBS2, OBS3, OBS4, OBS5, OBS6, and OBS10 are acquired simultaneously with 3-D P-cable data acquisition (shown in green in Figure 1b). At these sites, direct arrivals from different shot lines (plotted in green in Figure 1b) are used to constrain OBS location and water column velocity. A quality check of the relocated positions of an OBS can be done by applying the traveltimes correction for the water column. After the correction has been applied, direct arrivals should look flat, as the effect of water column with offset has been removed (Figure 2b). A band-pass filter is applied to the data set to improve the signal quality of the OBS seismic by removing high-frequency noise. Corner frequencies in a band-pass filter are selected depending upon visual inspection of the noise level in each data set. Selected frequencies in different OBS stations for low cut and high cut in the band-pass filter are between 10–20 and 200–250 Hz, respectively. Noise removal makes picking different reflection arrivals relatively easier compared to noisy data (Figures 2c and 3a).

The orientation of horizontal components is different from the inline and crossline directions (Exley et al., 2010). Therefore, for shear wave velocity analysis from the horizontal components of a seismogram, the two components recorded by a seismometer need to be rotated properly (Brown et al., 2002; Gaiser, 1999) so that two horizontal axes of the seismograms will be aligned to inline and crossline directions of the acquisition. This improves the quality of PS sections and makes picking of PS reflection



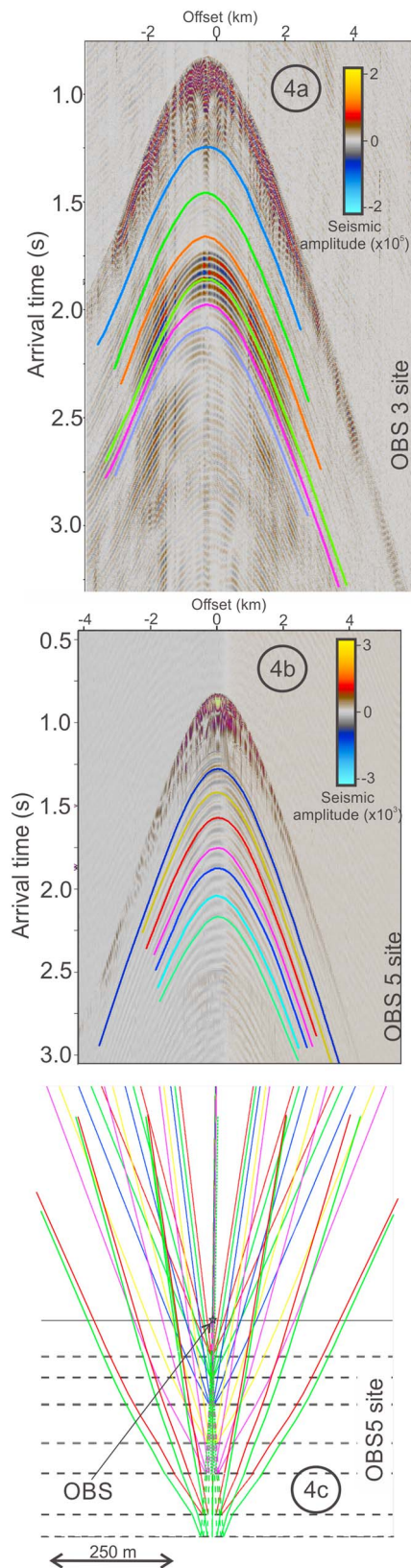


**Figure 4.** (a, b) PS records at sites OBS3 and OBS5 along with picked PS reflection arrivals. (c) Raypaths for *S* waves in the inverted model at site OBS5.

arrivals easier (Bünz et al., 2005; Kumar et al., 2007). We further apply a band-pass filter to improve the quality of a PS section. Converted PS waves have significant energy in the lower frequencies as they travel for longer times as compared to reflected PP waves. The *S* wave velocity is very low (<0.1 km/s) in the near-seafloor unconsolidated sediments, and thus, we observe ringing in the PS section (Richardson et al., 1991; Figure 4). Applying a low-cut frequency band-pass filter (<15 Hz) constitutes a good compromise of removing some of the ringing but preserving useful data in PS sections.

## 4. Methodology

### 4.1. *P* Wave Velocity Model

OBS data have been widely used to study gas hydrates (Hobro et al., 1998; Katzman et al., 1994; Posewang & Mienert, 1999; Song et al., 2018; Spence et al., 1995). Different methods have been used to derive velocity models using OBS data (Kumar et al., 2007; Shinohara et al., 1994; Zelt & Smith, 1992; Zillmer et al., 2005). Most of the methods used for estimating seismic velocities are either ray tracing (Červený, 2001; Julian & Gubbins, 1977; Virieux & Farra, 1991; Wang & Houseman, 1995) or grid-based methods (Nakanishi & Yamaguchi, 1986; Qin et al., 1992; Rawlinson & Sambridge, 2004; Vidale, 1988). We need good ray coverage to get efficient solutions from most grid-based tomographic or finite difference methods (Rawlinson et al., 1998). Based on ray coverage and separation between OBS stations, we find the ray tracing-based approach by Zelt and Smith (1992) suitable for our data set. Zelt and Smith (1992) described an efficient numerical solution of the ray tracing equation to estimate traveltimes for different source-receiver locations under different subsurface velocity models. RayGUI (Song & ten Brink, 2004) provides an interactive graphical user interface that makes it easier to perform velocity analysis using Rayinvr. We use RayGUI to invoke Rayinvr and derive velocity models at different OBS stations.

Different prominent reflection arrivals are picked from OBS data at each site (for example, seven picked reflection arrivals at site OBS3; Figure 2 c) to derive seismic interval velocities. We tried to pick the maximum possible number of reflection arrivals (seven to eight) at each OBS site keeping in mind the thickness and lateral continuity of individual layers. Velocity estimates for a thin layer derived from traveltimes inversion are not very reliable as the effect of a thin layer on the curvature of the traveltime curve is minimal and layers above this thin layer mainly determine the curvature. Broad combinations of velocity and depth can fit data for thin layers. Hence, we pick reflection arrivals keeping layer thickness greater than 20 m in order to improve accuracy of our results. We also tried to pick the same reflection arrivals at different OBS stations correlated through 2-D and 3-D seismic data (Figure 2c). In case the same reflection arrival is not strong enough laterally to pick traveltimes corresponding to far source-receiver offsets at different OBS stations, we picked another nearby strong reflection arrival.

The accuracy of a derived velocity model mainly depends on the accuracy of picked traveltimes along a reflection arrival and the farthest offset to where the picking can be done (Bickel, 1990; Lines, 1993). Picking at far offset traveltimes improves the confidence in the estimated velocity model since arrivals have significant moveouts (Dix, 1955; Yilmaz, 2001).

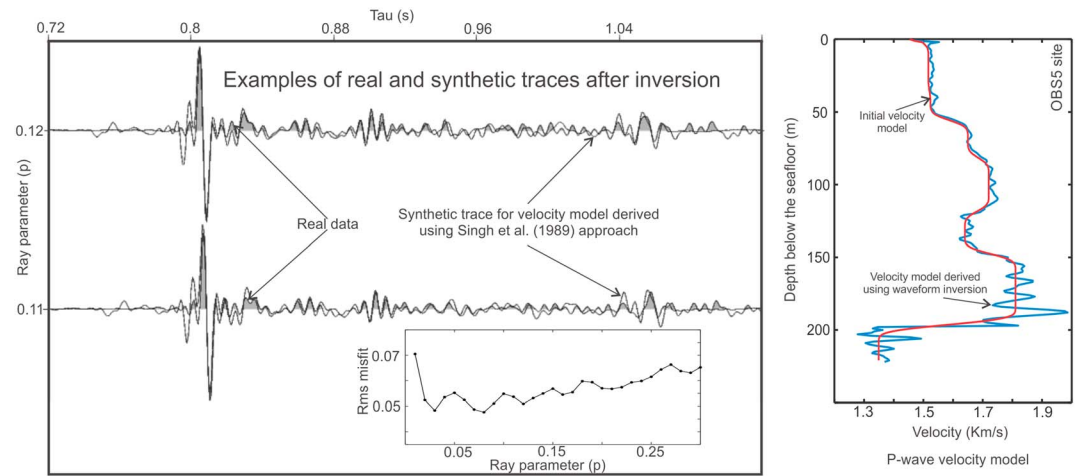


**Figure 5.** FWI-derived  $P$  wave velocity model at station OBS5. Two sample traces ( $p = 0.11$  and  $0.12$ ) have been shown that shows the match between real and synthetic data derived from inverted velocity model. Inset figure shows the variation of RMS misfit with ray parameter ( $p$ ).

However, the picks at far offsets have higher uncertainty as different reflection arrivals converge together and interfere to form a single phase. There is a trade-off between the accuracy of picked arrival times at far offset and the farthest offset traveltimes that can improve confidence in the velocity model (Lines, 1993). We do not pick far offset traveltimes that have high pick uncertainties ( $>1$  ms).

We invoke Rayinvr using RayGUI (Song & ten Brink, 2004; Zelt & Smith, 1992) to estimate traveltimes for a given velocity model, and the parameters in the velocity model are updated using the results obtained from the inversion (Figures 3 and 4). Velocities in the subsurface layers are assigned in a layer stripping approach starting at the top using traveltimes inversion of picked reflection arrival times (Figure 3). Different possible velocities and depths are tested in each layer to avoid the convergence of inversion to a local minimum. The process is repeated until we achieve a global minimum misfit between the traveltimes corresponding to picked and modeled reflection arrivals. For almost all picked reflection arrivals, the RMS misfit between modeled and picked traveltimes is less than 1 ms.

The resolution of  $P$  wave velocity model obtained using traveltimes inversion is quite low, depending on the number of reflection arrivals picked in the seismic data. This resolution can be significantly improved by applying full waveform inversion to the OBS data (Minshull & Singh, 1993; Singh et al., 1993; Westbrook et al., 2008; Xia et al., 1998). Depending on the type and the quality of the data set, several 1-D (Korenaga et al., 1997; Pecher et al., 1996; Westbrook et al., 2008; Xia et al., 1998) and 2-D full waveform inversion (Delescluse et al., 2011; Jaiswal et al., 2012; Wang et al., 2018) approaches have been used in the past to study the distribution of gas hydrates. In this study, OBS stations are not spaced closely enough to have overlap of raypaths in layers below the seafloor; hence, 1-D full waveform inversion is more suitable for this data set. We apply a downward continuation approach based on a 1-D full waveform inversion method (FWI; Singh et al., 1993; Westbrook et al., 2008) at station OBS5 in order to estimate the detailed variation of seismic velocities, especially near the BSR (Figure 5). A source wavelet is extracted using primary and multiple reflections from the seafloor (Singh et al., 1993). We use the velocity model obtained from traveltimes inversion of picked reflection arrivals to estimate the initial reflectivity function (Kemtett & Kerry, 1979; Pecher et al., 1996) and assume a fixed relationship between  $P$  wave velocity and density (Hamilton, 1978). Synthetic seismic data are obtained using a convolution operation between a source wavelet and reflectivity function (Kemtett & Kerry, 1979). Real data are matched with the synthetic data in frequency slowness domain (Sheriff & Geldart, 1982). We start by matching the seafloor reflection in synthetic and real data and with a downward continuation approach; the  $P$  wave velocity model is updated in successive iterations to reduce the misfit to a minimum (Singh et al., 1993). The RMS misfit for different values of  $p$  is in between 0.045 and 0.07 (Figure 5). The RMS misfit shows a small inconsistent increase with offset (Figure 5). The low RMS misfit between the real and synthetic traces in tau- $p$  domain ensures the accuracy of derived velocity model.

#### 4.2. *S* Wave Velocity Model

A *P* wave velocity model is prerequisite to derive an *S* wave velocity model from converted PS waves (Binz et al., 2005; Westbrook et al., 2008). In order to constrain *S* wave velocity from converted waves, it is necessary to correlate picked reflections in a PP section with reflections in the corresponding PS section (Kumar et al., 2007; Westbrook et al., 2008). Accuracy of the *S* wave velocity model depends on the reliability of this correlation (Westbrook et al., 2008). Different methods are used to correlate events in PP and PS sections. An approach to match events in PP and PS by visual correlation of seismic signatures or selection of events from a limited number of picked events in the absence of OBC data is widely used (Dash & Spence, 2011; Exley et al., 2010; Satyavani et al., 2016; Westbrook et al., 2008). In order to correlate events precisely, a semblance-based approach has been used (Appendix A). The basic premise behind this approach is the fact that the curvature of PS reflection arrivals in traveltimes versus offset plot will match with the curvatures of the estimated PS traveltimes curves for an accurate *S* wave velocity model (Appendix A). Traveltimes corresponding to these PS reflection arrivals are picked (Figure 4), and uncertainties associated with the velocity model are analyzed using Rayinvr. The resulting *S* wave velocity models have less than 3-ms RMS misfit in picked and modeled PS traveltimes and thus give a good estimate of shear wave velocities in the subsurface.

#### 4.3. Gas Hydrate and Free Gas Saturation Modeling

A number of empirical relations and rock physics models exist that allow us to estimate gas hydrate saturation from seismic velocity. Models predicting gas hydrate saturation from velocity data range from average traveltimes models that use simple empirical relations (Wood, 1941; Wyllie et al., 1958) to the more complex, rock physics-based models that account for the pore-scale interaction between gas hydrate, fluids, and sediment matrix (Carcione & Tinivella, 2000; Chand et al., 2006; Ecker et al., 1998, 2000; Helgerud et al., 1999; Jakobsen et al., 2000). The effect of gas hydrates in sediments on seismic velocities is more complex and cannot be precisely estimated using simple empirical models since the behavior of hydrate forming a composite with sediment matrix changes with hydrate saturation and mode of formation (Chand et al., 2006; Minshull & Chand, 2009). The rock physics-based methods incorporate the pore-scale interactions and variations in hydrate-sediment morphology. These methods can effectively account for the hydrate-sediment microstructure (e.g., whether hydrate forms as a part of sediment matrix, forms in the pore space, or forms as filler in fault gaps). Hence, the patterns of velocity variation with hydrate saturation vary between different models of hydrate formation. Therefore, one has to choose the model based on various parameters such as host sediment type, changes in *P* and *S* wave velocity, and presence of faults to incorporate these effects (Chand et al., 2006; Marín-Moreno et al., 2017). The presence of hydrate in sediments increases the seismic *P* wave velocity but may or may not increase *S* wave velocity compared to the background velocity, depending on the amount of hydrate present and their form of distribution in the pore spaces. Hence, the difference between the background velocity and the observed velocity changes can be used to find the gas hydrate saturation (Chand et al., 2004).

The SCA (Willis, 1977)/DEM theory (Nishizawa, 1982) predicts the effective stiffnesses of an aggregate of randomly oriented crystals where hydrate is incorporated (Jakobsen et al., 2000). Since DEM preserves the initial connectivity of phases (Sheng, 1990), the combination can produce a composite that is biconnected at any porosity and new components such as hydrates can be introduced to the effective medium. The model can therefore handle the case where gas hydrates are present as an unconnected phase within pore spaces (Case 1) or the case where gas hydrates form as a part of the sediment matrix (Case 2). In Case 1, the effect of increment in gas hydrates saturation is adjusted with equal decrease in water saturation along with an effective change in sediment-water composite stiffness using DEM, whereas in Case 2, the method is similar but the starting effective medium is a clay-gas hydrate composite representing hydrate as part of the sediment matrix. Since an increase in *S* velocity is observed above the BSR, hydrate formation as part of sediment-hydrate composite is inferred for a given gas hydrate saturation and we have therefore employed this method to calculate gas hydrate saturations in the present study. This model has been used previously to study gas hydrate saturation from the seismic velocities in nearby locations (Hustoft et al., 2009; Westbrook et al., 2008). The effect of individual fracture properties is not studied here since the seismic data used only give an estimate of the effective properties of the medium lying in between the source and the receiver, which are several orders of magnitude larger than the size of the fractures. The existence of pure



hydrate-filled fractures can therefore result in overprediction of hydrate saturation depending on the porosity of pure hydrate formed, but it is partly accounted for in the uncertainty estimates.

Lithology and porosity are very important parameters to estimate seismic velocities in a medium. The porosity parameter becomes even more important in the shallow subsurface as porosity changes rapidly at these depths. Accurate lithology and porosity parameters are prerequisite to estimate gas hydrate saturation in marine sediments. We have very limited information available about these parameters in the area. Chemical, X-ray powder diffraction (XRD), and grain size analysis of a gravity core in one of the nearby sites (Hustoft et al., 2009) show 25% clay, 39% mica, 24% quartz, 5% feldspar, and 7% calcite as the sediment composition. The sediment composition from this site (Hustoft et al., 2009) is used in the SCA/DEM to derive seismic velocities in a water-saturated medium. As a simple approach, lithology of the near-surface sediments is considered the same as the lithology of the deeper sediments as well. We use porosity data obtained from ODP well logging to get a smoothed porosity variation with depth. Differences in lithologies at Vestnesa Ridge and the ODP site should be considered to get a better overview of porosity variation with depth. Hustoft et al. (2009) used a porosity profile in which variations in porosity due to changes in lithologies at the ODP and study sites are considered. The porosity profile used by Hustoft et al. (2009) is also used in this paper as our study area is proximal to the presented in Hustoft et al. (2009). Sediment connectivity and orientation of microfractures have strong impacts on seismic velocity. We chose the sediment connectivity parameter, which includes the effect of microfractures that satisfy the range of seismic velocities derived by OBS data.

## 5. Uncertainty Analysis

The uncertainties of the velocity analysis are mostly associated with the accuracy of picking different reflection arrivals from OBS data (Bünz et al., 2005; Plaza-Faverola et al., 2010). Pick uncertainty depends on the quality of the data set, as a seismic reflection can be picked with high certainty in a good quality data set. Data sets with high-frequency content, high sampling interval, low signal-to-noise ratio, etc., will have low pick uncertainty. The quality of source and receiver mainly decides these parameters. Seismic signals generated by seismic sources in this study have high centroid frequencies (>100 Hz), and the OBS data therefore have higher signal-to-noise ratio than typical seismic sources. However, there is poor signal-to-noise ratio after a certain depth below the BSR. This can be due to high attenuation in the free gas zone and limited penetration of P-Cable data. Hence, we only model one layer below the BSR. Sampling rate of the recorded data is quite high (Table 1). Certain parameters related to source-receiver geometries like seafloor depth, source-receiver offset, horizontal offset between shot line, and OBS location also affect the pick uncertainty. Pick uncertainty is higher for large source-receiver offsets as reflection arrivals merge at larger offsets; thus, it is difficult to track a given phase. Reflection arrivals merge at shorter offsets with an increase in depth. Water depth in the study area is around 1.2 km, and this allows us to pick a given reflection arrival up to 2–4-km offset depending on the strength of the arrival. Pick uncertainty can be further constrained by picking upper and lower bounds of the picked reflection arrivals, thus providing the uncertainty parameter for each traveltimes pick in Rayinvr. This offset varying pick uncertainty helps in giving a suitable weightage to every traveltimes pick and thus constrains the derived velocity model well. A fixed constant is typically given as an uncertainty parameter in the input model (Plaza-Faverola et al., 2010). In our case, we have only picked those traveltimes where our uncertainty about the pick is less than 1 ms.

There are also uncertainties in the estimated velocity model due to the simplistic assumption of a subsurface where layers are isotropic and homogeneous with no horizontal variation along a given layer. Picked traveltimes along a curvature will not follow the curvature as predicted by the velocity model if there is horizontal variation in seismic velocities (Thomsen, 1986; Thomsen, 1999). It is hard to study small horizontal velocity variations along a layer with the limited available data set, and there will always be misfit between the picked traveltimes and estimated traveltimes due to inherent complexity of the subsurface (Chitū et al., 2008).

In order to study the sensitivity of the seismic velocity model to all these parameters, we analyze the variation of RMS misfit with change in the velocity model using the approach documented by Katzman et al. (1994). Perturbation of a velocity model increases the RMS misfit between the modeled and picked traveltimes as estimated seismic velocity models have least RMS misfit. In order to study the uncertainty in a

modeled depth or velocity parameter, we perturb either parameter so that the RMS misfit increases and exceeds the pick uncertainty. In some cases, where the modeled traveltimes fit well with the picked traveltimes, we need very strong perturbation in order to increase the RMS misfit to 2 ms. On average, we find that we need to perturb the velocity model by approximately 0.06 km/s in order to increase the RMS misfit to 2 ms. Considering the good fit between modeled and picked traveltimes attained from the layer-stripping approach, uncertainty in the velocity estimates may be less than the uncertainty estimated using the Katzman et al. (1994) approach.

Uncertainties associated with the *S* wave velocity model are higher than uncertainties in the *P* wave velocity model, because we need very far offset traveltime picks to achieve good *S* wave velocity estimates. PS waves are reflected at a very low angle (Figure 4c), as *S* wave velocities are low compared to *P* wave velocities in the near-surface sediments. In order to achieve the significant offsets required to perform *S* wave velocity modeling, we picked far offset converted PS waves for different seismic reflection arrivals. However, far offset picks are always associated with high uncertainties due to high noise level and interference between different reflection arrivals. Pick uncertainty in picked PS traveltimes is high (up to 3 ms) leading to high uncertainty in the *S* wave velocity model (0.1 km/s).

Uncertainties in velocity models propagate to the uncertainties in gas hydrate and free gas saturation estimates. Uncertainty in gas hydrate saturation estimates also comes from the uncertainties in the lithology, presence of faults/microfractures, and porosity profiles at the study site. We derive porosity and lithology profiles from the limited information available about these parameters in the region. These approximations generate uncertainties in the base velocity profile generated for water-saturated sediments using the SCA/DEM modeling approach. The velocity model in a layer beneath the low-velocity zone below the BSR gives us an idea about the accuracy of estimated base velocity profiles and the extent of velocity deviations in layers near the BSR (Bünz et al., 2005; Hustoft et al., 2009). However, due to a limited signal-to-noise ratio, it is hard to model seismic velocities in this layer. The uncertainties in sediment composition, porosity changes, etc., are calculated using the maximum changes observed in sediment composition and porosity at corresponding depths (Hustoft et al., 2009). This uncertainty is converted to velocity uncertainties and used in the inversion algorithm based on McKenzie and O'Nions (1991) approach (Chand et al., 2006). We calculate uncertainties that arise in gas hydrate and free gas saturation estimates from the SCA/DEM modeling due to uncertainties in the velocity models, porosity, and lithology profiles (Chand et al., 2006).

## 6. Results

Interval *P* wave velocity models are estimated in this study for six to seven layers below the seafloor at 10 OBS locations using traveltime inversion (Figures 1, 6, and 7). The *P* wave velocity in the water column ranges from 1.463 to 1.468 km/s at different OBS stations. There are no significant differences in the *P* wave velocity beneath all OBS stations in the first 40 m below the seafloor—seismic velocities for this interval are between 1.5 and 1.537 km/s. There are some differences in *P* wave velocities beneath different OBS stations between 40- and 80-m depths below the seafloor. Seismic velocities at OBS3 (1.62 km/s) and OBS5 (1.66 km/s) are higher than seismic velocities (<1.60 km/s) at other OBS stations. *P* wave seismic velocities increase by around 0.1–0.15 km/s beneath almost all stations (Figure 7a) across the ~0.2-Ma discontinuity (shown in the Figure 2c; Plaza-Faverola et al., 2015) around 70–80-m depth below the seafloor. *P* wave velocities in the 80- to 130-m depth range below the seafloor vary considerably beneath OBS stations. We find low seismic velocity (1.58 km/s) northeast of a fault (yellow dashed line in Figure 1c) at OBS3 and very high seismic velocity (1.73 km/s) southwest of the fault at OBS5 compared to the seismic velocities (1.62–1.66 km/s) at other OBS sites. In the 130- to 155-m depth range, we find small variations in *P* wave velocities (1.65–1.70 km/s) beneath different OBS stations. Significant *P* wave velocity differences (1.73–1.82 km/s) are observed in the layer above the BSR. OBS stations southwest of the fault (Figure 1c), that is, OBS5 and OBS6, show the highest seismic velocities (1.82 km/s), whereas OBS stations northeast of the fault, that is, OBS2 and OBS3 sites, show the lowest seismic velocities (1.736–1.743 km/s) in this layer. Other sites closer to the ridge crest, that is, OBS1 and OBS4, also show higher seismic velocities (1.80 km/s) compared to seismic velocities (1.74–1.76 km/s) at OBS sites away from the ridge crest, that is, OBS7, OBS8, and OBS9. At site OBS10 on the northeastern flank of the ridge, the seismic velocity (1.757 km/s) does not show any anomalous change in this layer. The depth of the BSR in the study area (Figures 2, 7a, and 8) ranges between 190

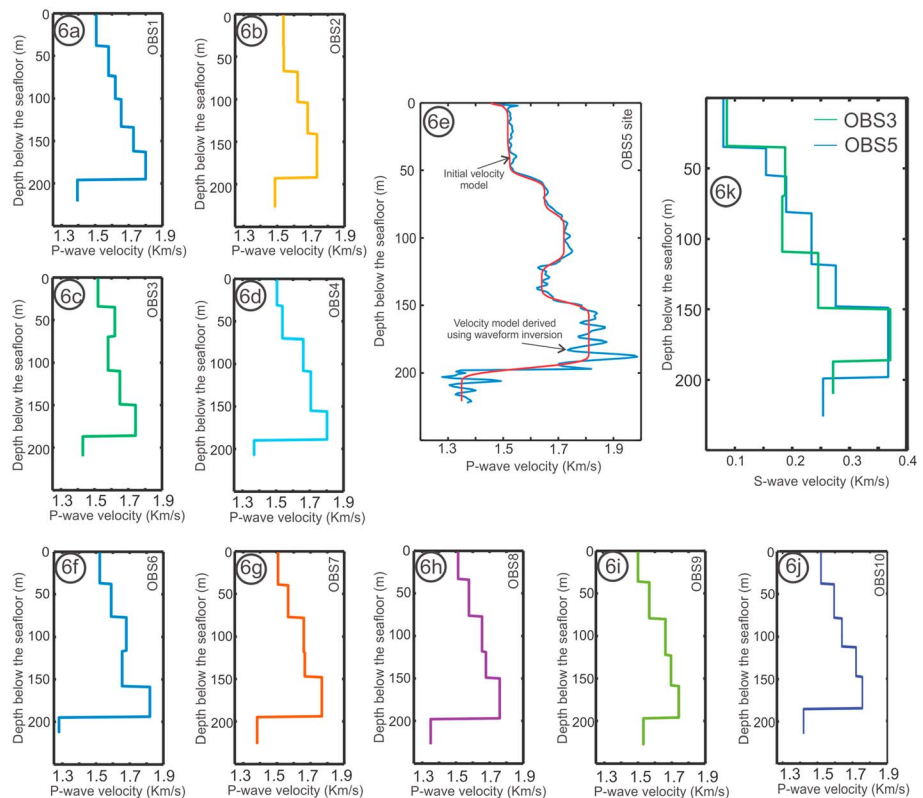


**Figure 6.** *P* and *S* wave velocity estimates using traveltime inversion at different OBS sites. Blue curve in Figure 6e shows the velocity model derived using 1-D FWI approach.

and 196 m below the seafloor across all OBS stations. Variations in the *P* wave velocities (1.28–1.53 km/s) at different OBS stations are highest in the layer below the BSR. One of the OBS stations southwest of the fault (OBS6) shows the lowest seismic velocity (1.28 km/s). At other OBS stations, seismic velocities are in the 1.35–1.40 km/s range, except at sites OBS2 (1.49 km/s) and OBS9 (1.53 km/s), where higher seismic velocities are observed. *P* wave velocities estimated using FWI increase the resolution of *P* wave velocity model significantly. At site OBS5, very high *P* wave velocities (>1.95 km/s) are observed in a very narrow interval above the BSR.

*S* wave velocities have been estimated at sites OBS3 and OBS5 (Figure 6k). Low *S* wave velocities (<0.2 km/s) are observed at shallow depths, while velocities increase sharply to ~0.37 km/s near the BSR depth. *S* wave velocities decrease beneath the BSR to 0.272 and 0.252 km/s at OBS3 and OBS5, respectively. There are also significant differences in *S* wave reflectivity patterns in the GHSZ for OBS stations on different sides of the fault (yellow dashed line in Figure 1c). There are strong reflections in an interval (~50–60 m) above the BSR in the PS section at site OBS3 (Figure 4a), whereas there are no distinct reflections at site OBS5. PS records in other instruments also show similar differences (Figure 9), which removes the possibility of an instrument related artifact. There are continuous PS reflections at OBS stations southwest of the fault (OBS5 and OBS6), whereas strong distinct PS reflections (Figures 4 and 9) occur in the GHSZ at OBS stations northeast of the fault (OBS1, OBS2, and OBS3).

## 7. Discussion

### 7.1. Presence of Gas Hydrates and Free Gas

We have estimated *P* wave velocity profiles at 10 OBS stations (Figures 6 and 7), *S* wave velocity profiles at two OBS stations (OBS3 and OBS5), and applied FWI for a detailed investigation of the *P* wave velocity at site OBS5. We calculated background seismic velocities assuming water-saturated sediments using the SCA/DEM approach (Figure 8a) and compared these with OBS velocity models. There are increases in *P*



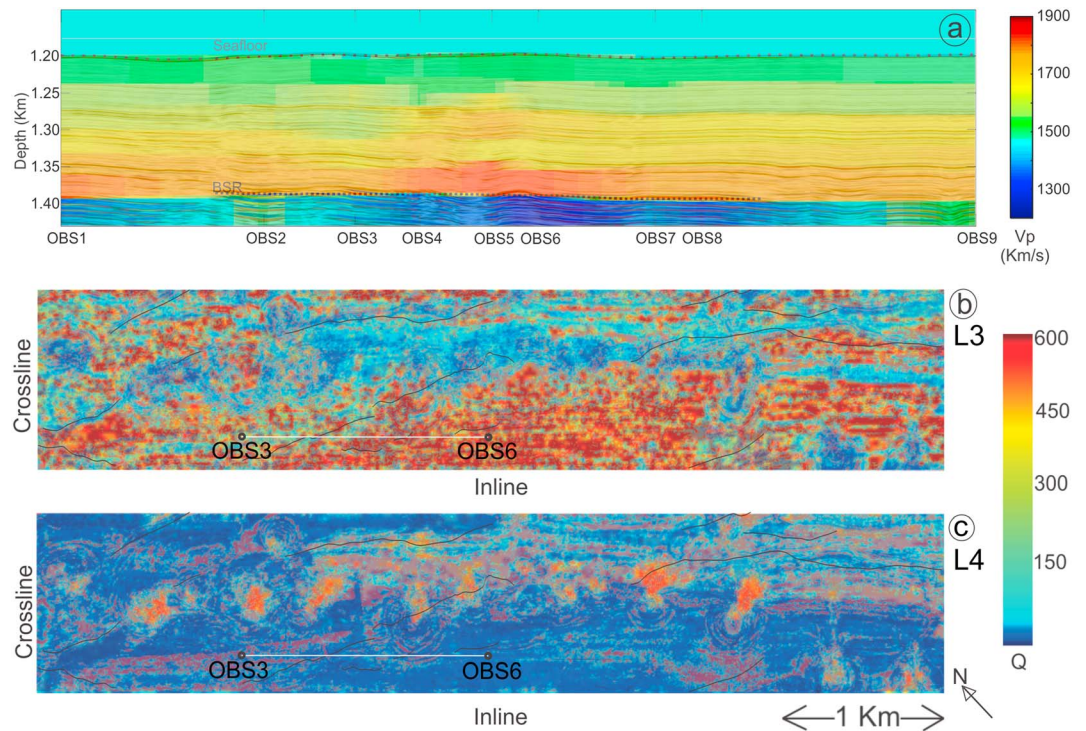


**Figure 7.** (a) Overlay of P-cable seismic data and interpolated  $P$  wave velocity model. Seismic  $Q$  map (modified from Singhroha et al., 2016) in a layer above the BSR (b) and below the BSR (c). White line shows the transect from OBS3 to OBS6.

wave velocities ( $\sim 0.04$ – $0.13$  km/s) and  $S$  wave velocities ( $\sim 0.1$  km/s) above the BSR compared to background velocities. A detailed  $P$  wave velocity model derived from FWI at site OBS5 shows an increase ( $\sim 0.3$  km/s) and decrease ( $\sim 0.2$ – $0.4$  km/s) in  $P$  wave velocities above and below the BSR, respectively. These variations in seismic velocities are well above model uncertainties. Considering the contourite depositional setting at the study site where strong changes in seismic velocities due to lithological changes are unexpected, increases and decreases in seismic velocities above and below the BSR, respectively, can be attributed to the presence of gas hydrates and free gas in the pore space of the sediments (Goswami et al., 2015; Hustoft et al., 2009).

## 7.2. Gas Hydrate and Free Gas Saturation

We estimate gas hydrate and free gas saturations based on difference between estimated and background seismic velocities using the SCA/DEM approach (Figure 8). We further constrain gas hydrate and free gas saturation estimates at sites OBS3 and OBS5 using  $S$  wave velocity analysis. Uncertainties are significantly lower (less than half) in saturation estimates derived from combined analysis of  $P$  wave and  $S$  wave velocities compared to uncertainties in saturation estimates derived from the  $P$  wave velocity alone (shown as error bars in Figures 8b and 8c). We do not find any significant gas hydrate saturation ( $<0$ – $2\%$ ) in the first 50 m of sediments at any OBS site except at OBS3 ( $0$ – $5\%$ ). In the layers between 50 and 100 m below the seafloor, we do not estimate significant gas hydrate saturations at sites OBS1, OBS2, and OBS10 ( $<0$ – $2\%$ ). Beneath the other stations, gas hydrate saturations vary between 3 and 10%. In the layers approximately 100 to 150 m below the seafloor, gas hydrate saturations vary between 0 to 10% at all OBS stations. It is difficult to study low gas hydrate saturations ( $<5$ – $10\%$ ) from seismic velocity analysis as uncertainties are quite high (shown by error bar in Figure 8). Small variations in seismic velocities may also be due to minor changes in sediment properties rather than the presence of gas hydrates. However, the gas hydrate saturation in a layer close to the base of the GHSZ is high and well above the uncertainty limit. In the layer directly above the BSR, we estimate highest gas hydrate saturations ( $\sim 18\%$ ) at OBS stations that are southwest of the fault (OBS5 and OBS6). We also estimate higher gas hydrate saturations ( $\sim 16\%$ ) at OBS4, which lies on the fault, and at OBS1, which is close to the ridge crest (Figure 1), compared to other stations where gas hydrate

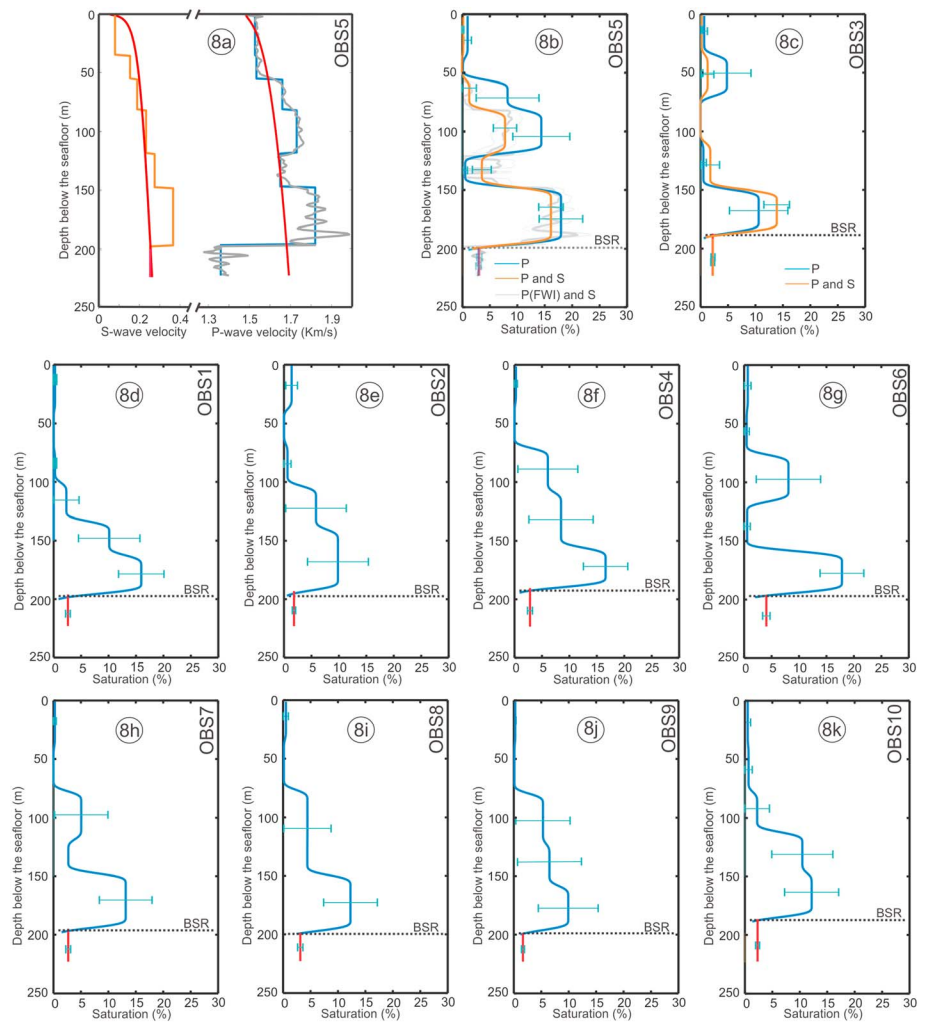


**Figure 8.** (a) Traveltime inversion-derived (shown in blue) and FWI-derived (shown in gray) *P* wave and *S* wave velocity model at site OBS5 plotted along with background velocity model (shown in red) derived using the SCA/DEM approach. (b) Saturation estimated using different possible combination of velocity models at site OBS5. (c–k) Saturation estimates at different OBS locations using *P* wave velocity model.

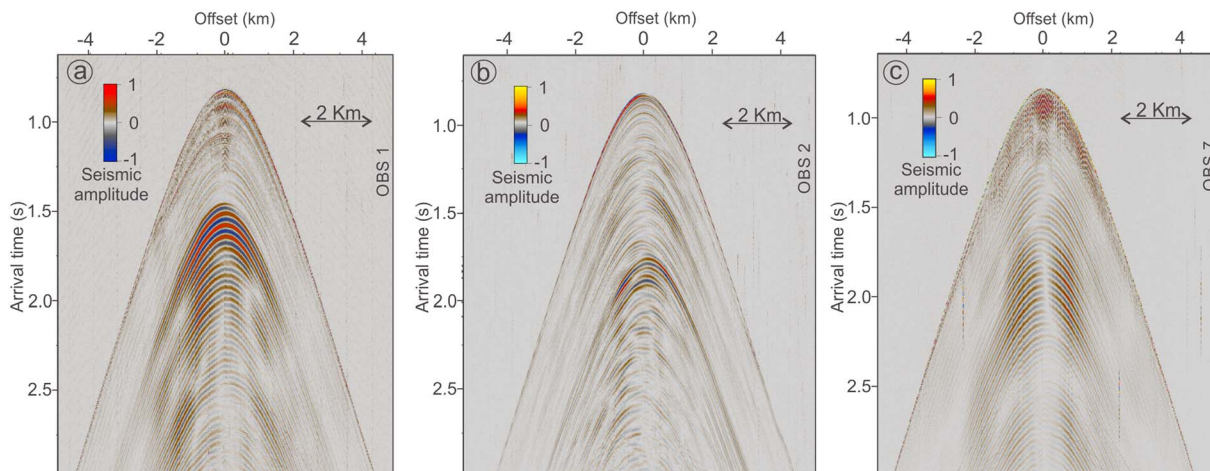


**Figure 9.** PS data recorded at different OBS stations.

saturations are between 10 and 13%. At OBS stations northeast of the fault (OBS2 and OBS3) and at station OBS9, we find low gas hydrate saturations (~10%) in this layer. Free gas saturations vary from 1.5 to 4.1% at OBS stations along the ridge. However, OBS stations that are southwest of the fault (OBS5 [3.0%], OBS6 [4.1%], and OBS8 [3.1%]) have considerably higher free gas saturations compared to the rest of the stations where free gas saturations vary from 1.5 to 2.8%.

Gas hydrates often occur in thin layers of high gas hydrate saturation as observed from drilling at different locations (Collett et al., 2012, 2014). The velocity model from FWI gives finer details about the subsurface velocities (Figure 6e). High *P* wave velocities in a narrow zone can potentially be due to high gas hydrate saturation zones in narrow intervals (Figures 8a and 8b). The high *P* wave velocity (~2.0 km/s) observed just above the BSR indicates the higher gas hydrate saturation (>20%) near the base of the GHSZ. Combined analysis of the FWI-derived *P* wave velocity and the *S* wave velocity at site OBS5 (Figures 8a and 8b) helps in detecting gas hydrates in thin layers (especially between 125- and 150-m depths below the seafloor).

### 7.3. Geological Controls on Gas Hydrate and Free Gas Distribution

Gas hydrate and free gas saturation estimates vary along the ridge. The topography of Vestnesa Ridge favors the accumulation of free gas near the ridge crest (Hustoft et al., 2009; Singhroha et al., 2016), and thus, we expect that the gas hydrate saturation will be higher for OBS stations closer to the ridge crest. Velocity models from Goswami et al. (2015) at two locations on Vestnesa Ridge also show that the gas hydrate saturation is higher in the GHSZ just above the BSR for the location closest to the ridge crest. In the present study, we observe higher gas hydrate saturations (>15%) at the OBS stations near the crest of the ridge, except at stations OBS2 and OBS3.

Low gas hydrate saturations derived from *P* wave velocity models at OBS2 and OBS3 (around 10%) near the BSR depth has also been predicted by Singhroha et al. (2016) using seismic *Q* analysis of high-resolution P-cable seismic data (Figure 7). Faults and discontinuities demarcate *Q* anomalies in the region and the differences in *Q* can be due to differences in gas hydrate and free gas saturations across the fault (Figures 7b and 7c). We also find significant differences in *P* wave velocities across the fault from OBS3 to OBS5 (Figure 7). Low gas hydrate and free gas saturations near the BSR at sites northeast of the fault (OBS2 and OBS3; Figure 1c) compared to sites southwest of the fault (OBS5 and OBS6) can potentially be due to the presence of fault, which acts as a fluid migration pathway or shuts off the supply of gas-rich fluids to adjacent strata. The ridge topography favors the migration of gases toward the ridge crest; however, faults can play a significant role in controlling the upslope migration of gases. Faults can be permeable and lead to leakage of gases toward permeable layers further up in the stratigraphic section, or they can be sealing (due to the displacement of permeable routes by the fault) and block any upslope migration of gases, thus making the region in the upslope direction gas deprived. Hence, differences observed in estimated gas hydrate and free gas saturations across the fault can be due to differences in the availability of gas.

The distribution of gas hydrates on Vestnesa Ridge is very typical of a deep marine setting, where highest hydrate saturations are found directly above the BSR (Bünz et al., 2005; Tréhu et al., 2004; Westbrook et al., 1994). In these settings, free gas is migrating into the GHSZ right above the BSR where it forms gas hydrate. Ongoing sedimentation and burial moves the deepest gas hydrate accumulations out of the GHSZ, leading to gas hydrate dissociation. Gas released during this process can migrate back into the GHSZ reforming hydrates (Hyndman & Davis, 1992; Kvenvolden & Barnard, 1983; Minshull et al., 1994; Minshull & White, 1989; Nole et al., 2018). This process develops a typical hydrate distribution with depth that we see today (Bhatnagar et al., 2007). Higher gas hydrate saturation estimates obtained using FWI above the BSR (Figure 8b) further support this theory (Pecher et al., 1996). This type of diffusive flow is the primary mode of gas hydrate formation in regions that are away from permeable faults or fractures (Daigle & Dugan, 2011; Liu & Flemings, 2011; Rempel, 2011). In places close to permeable faults or fractures, advective methane flux can also contribute to the gas hydrate formation (Davie & Buffett, 2001, 2003; Rempel & Buffett, 1997; Xu & Ruppel, 1999). Faults can act as conduits for fluid flow, and the fluid passing through faults can create a series of fracture networks if the fluid pressure exceeds a certain value (Stranne et al., 2017). This process is dominant in fluid flow systems like gas chimneys (Liu & Flemings, 2007). In this study, OBS stations are away from gas chimneys where strong advective fluxes are expected; therefore, we expect



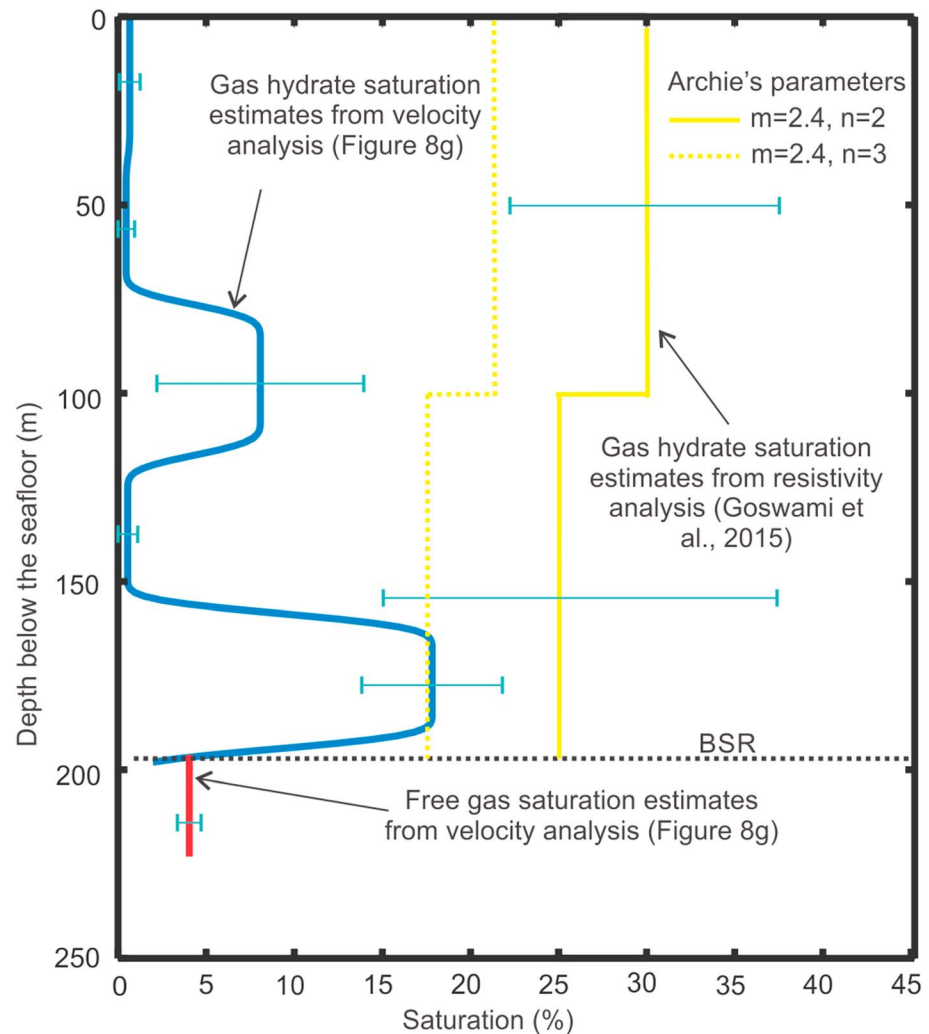


**Figure 10.** Gas hydrate saturation estimates from velocity analysis of OBS6 and resistivity analysis of CSEM data (Goswami et al., 2015). Yellow line and yellow dashed line show the variation of gas hydrate saturation profile with variation in Archie's parameter  $n$  (saturation exponent).

gas hydrate saturations derived at OBS stations to be reflective of diffusive fluid flow and slower rates of gas hydrate accumulation. However, earlier studies and gas hydrate saturation estimates derived from electromagnetic (EM) data may suggest otherwise (Goswami et al., 2015).

Gas hydrate saturations estimated by velocity analysis of multicomponent seismic data are significantly lower than gas hydrate saturations estimated by the EM method (Figure 10; Goswami et al., 2015). Goswami et al. (2015) predict 30% gas hydrate saturation in 0–100-m depth and 20–30% gas hydrate saturation in 100–200-m depth outside the gas chimney. Higher gas hydrate saturation estimates using resistivity methods compared to gas hydrate saturation estimates using seismic velocity analysis of multicomponent seismic data have been reported in several studies at different sites (Cook et al., 2010; Lee & Collett, 2009; Weitemeyer et al., 2011). The presence of free gas in coexistence with gas hydrates in the GHSZ increases the resistivity of a medium and decreases the  $P$  wave velocity, which may explain the discrepancy in gas hydrate saturation estimates derived from seismic velocity analysis and resistivity analysis. Goswami et al. (2015) investigate this possibility and suggest the presence of coexisting gas hydrates and free gas in gas chimneys and even at sites away from gas chimneys. However, the anisotropic distribution of gas hydrates can also explain the differences in gas hydrate saturations estimated from the  $P$  wave velocity and resistivity analysis. This study and the study by Goswami et al. (2015) assume an isotropic gas hydrate distribution in a medium.

Gas hydrate saturations derived from seismic velocity and resistivity analysis normally overestimate the amount of gas hydrate due to the assumption of isotropic pore filling gas hydrate morphology (Lee & Collett, 2009). Seismic wavelengths used in seismic exploration surveys are long (normally  $>10$  m), and small-scale heterogeneities in the distribution of gas hydrates have a small effect on seismic velocities (Lee & Collett, 2009). The variation in gas hydrate saturation derived from seismic velocity analysis is small ( $<10$ – $20\%$ ) due to changes in the gas hydrate morphology from pore filling to grain displacing (Ghosh et al., 2010). However, this difference can be large ( $>400\%$ ) if the gas hydrate saturation is estimated using resistivity methods with an assumption of an isotropic pore filling gas hydrate distribution in a gas hydrate-filled fracture deposit (Lee & Collett, 2009; Lee & Collett, 2012). Archie's parameters, that is,  $a$  (cementation exponent),  $m$  (cementation factor), and  $n$  (saturation exponent), used in Archie's equation by Goswami et al. (2015) for estimating gas hydrate saturation vary strongly due to anisotropy in a medium (Kennedy et al., 2001; Kennedy & Herrick, 2004; Lee & Collett, 2009). Different anisotropic parameters like the orientation of fractures and interconnectivity within fractures have a big effect on the resistivity estimates (Kennedy et al., 2001; Kennedy & Herrick, 2004; Lee & Collett, 2009). For example, gas hydrate saturation estimates from resistivity measurements in gas hydrate-filled vertical fractures can be 5 times higher than the actual gas hydrate concentration (Lee & Collett, 2012). Archie's parameters also vary with changes in the gas hydrate saturation, and variations in  $n$  are bigger than variations in  $m$  due to anisotropy (Kennedy & Herrick, 2004; Lee & Collett, 2009). The value of  $n$  can be between 1.25 and 7, depending on an anisotropy in a medium (Kennedy & Herrick, 2004). Assuming an isotropic gas hydrate distribution, Goswami et al. (2015) use  $n = 2$  to estimate gas hydrate saturations. A recent study by Cook and Waite (2018) show that the use of  $n = 2$  overestimates the gas hydrate saturation and  $n = 2.5$  should be used as a default value for an isotropic gas hydrate distribution if independent estimates are not available. Lee and Collett (2009) recommend the use of  $n > 2.5$  for an anisotropic medium. Earlier studies in the Vestnesa Ridge suggest the presence of faults and fractures in the area (Bünz et al., 2012; Plaza-Faverola et al., 2015; Singhroha et al., 2016). Considering the possibility of a minor fraction of gas hydrates in fractures and faults, we use a value of  $n = 3$  in the Archie's equation, which fits well for velocity and resistivity analyses to estimate the gas hydrate saturation (Figure 10). The minor presence of gas hydrates ( $20$ – $30\%$ ) in fractures or faults will have a very small effect on gas hydrate saturations derived using seismic velocity analysis, and overall change in the gas hydrate saturation will be as small as  $1$ – $2\%$  (Ghosh et al., 2010). However, it changes gas hydrate saturation estimates from resistivity analysis by  $30\%$  (Figure 10). The use of  $n = 3$  gives the gas hydrate saturation estimate of  $13.8$ – $21.1\%$  in  $100$ – $200$ -m depth as opposed to gas hydrate saturation estimates of  $20$ – $30\%$  in the same interval for  $n = 2$ . Gas hydrate saturation estimates for  $n = 3$  ( $13.8$ – $21.1\%$ ) match well with the saturation estimates from seismic velocity analysis ( $10$ – $18\%$ ) in a layer above the BSR (Figure 8). There are still differences in gas hydrate saturation estimates from these two methods in the  $0$ – $100$ -m depth interval. These differences could be due to intersite variability. Significant differences in gas hydrate saturation estimates from EM data and seismic velocity analysis potentially hint toward the presence of gas hydrates in fractures in the region.

It is difficult to differentiate between the possibility of gas hydrates present in fractures and the coexistence of free gas and gas hydrates in the GHSZ using  $P$  wave velocity and resistivity data. Combining the analyses from  $P$  wave velocity models and resistivity data with  $S$  wave velocity models, seismic  $Q$  models and PS reflectivity can help us in differentiating between these two possibilities. We do not have resistivity models at all our OBS sites; however, we can analyze our results keeping in mind these two possibilities.

Changes in the PS reflectivity from continuous PS reflections (OBS5 and OBS6) to strong distinct PS reflections (OBS1, OBS2, and OBS3) occur across the fault (Figures 1c, 4, and 9). These differences in PS reflectivity can be due to differences in the geological settings. Considering that these changes occur across the fault, there is a strong possibility that these differences can be due to changes in the distribution of gas hydrates. The occurrence of free gas or layered gas hydrates in the GHSZ can potentially generate such effects. With the limited geological information in the area, it is difficult to argue in favor of the possibility of gas hydrate as layered deposits at OBS stations northeast of the fault. However, some of our results support the theory that free gas coexist with gas hydrates in the GHSZ at OBS station northeast of the fault (OBS3 site). The presence of free gas in the GHSZ will decrease the  $P$  wave velocity and  $Q$  but will have very little impact on the  $S$  wave velocity. No significant differences in  $S$  wave velocity estimates above the BSR across the fault (OBS3 and OBS5) favor the theory of the presence of free gas in

GHSZ (Goswami et al., 2015) at OBS station northeast of the fault (OBS3). The interval  $P$  wave velocity above the BSR is also significantly lower (1.74 km/s) at the OBS station northeast of the fault (OBS3) compared to the interval  $P$  wave velocity ( $>1.8$  km/s) at OBS stations southwest of the fault (OBS5 and OBS6).  $Q$  analysis also shows low  $Q$  values northeast of the fault compared to high  $Q$  values southwest of the fault in a layer above the BSR (Singhroha et al., 2016). The presence of free gas creates high seismic attenuation and thus low  $Q$  values are observed in sediments saturated with free gas. Geologically, the presence of free gas in the GHSZ in a contourite setting with good permeability and low gas hydrate saturations ( $<25\%$ ) seems unlikely as we can expect sufficient supply of water to form gas hydrate. Nevertheless, a recent study by Sahoo et al. (2018) shows that hydrate films can envelop free gas in the GHSZ even in sediments with good permeability. Sahoo et al. (2018) attributed differences in gas hydrate saturation estimates from resistivity and seismic observations to the presence of free gas in GHSZ as we observe in our study area (Goswami et al., 2015). Based on this theory and our results, we can hypothesize that gas hydrate saturations can be potentially similar across the fault (Figures 8b and 8c) and there can be differences in the amount of free gas trapped inside gas hydrate films across the fault leading to differences in  $P$  wave velocities above the BSR in the GHSZ. However, considering the fact that there are low free gas saturations below the BSR at OBS stations northeast of the fault (OBS2 and OBS3), as suggested by  $Q$  analysis (Singhroha et al., 2016) and  $P$  wave velocities (Figures 7 and 8), it is difficult to explain higher amounts of free gas trapped in the GHSZ at OBS station northeast of the fault (OBS3) compared to OBS station southwest of the fault (OBS5). Differences in the  $P$  wave velocity and similarities in the  $S$  wave velocity across the fault (OBS3 and OBS5) can also be due to similarity in the load bearing gas hydrate saturation and differences in the pore fill gas hydrate saturation. This is less likely to happen geologically as gas hydrates tend to become load bearing with increase in gas hydrate saturation (Minshull & Chand, 2009). In addition, it will be difficult to explain differences in seismic  $Q$  analysis (Singhroha et al., 2016) across the fault. We expect lower  $S$  wave velocity at OBS station northeast of the fault (OBS3) than OBS station southwest of the fault (OBS5). Similar  $S$  wave velocity ( $\sim 0.37$  km/s) observed above the BSR across the fault (OBS3 and OBS5) can potentially also be an artifact due to high uncertainty ( $\sim 0.1$  km/s) in  $S$  wave velocity estimates.

Results from different surveys and methods seem to favor the theory of the coexistence of free gas and gas hydrates northeast of the fault although we cannot rule out the possibility of the presence of gas hydrates in fractures, especially southwest of the fault. Although there are some nonuniqueness interpretation issues, with significant differences in different seismic properties ( $P$  and  $S$  wave velocity, seismic  $Q$ , and shear wave reflections in PS sections) across the fault (dashed yellow line in Figure 1c), we can say with high confidence that faults play an important role in the distribution of gas hydrates and free gas in the region (Figure 7).

## 8. Conclusion

We perform seismic velocity modeling at 10 OBS locations along the Vestnesa Ridge to study the gas hydrate saturation. We observe high interval  $P$  wave velocities (1.73–1.82 km/s) in a layer above the BSR and low interval  $P$  wave velocities (1.28–1.53 km/s) in a layer below the BSR. The depth of the BSR is around 190–196 m at different OBS stations. Results based on FWI suggest that the  $P$  wave seismic velocity can be higher than 1.95 km/s above the BSR at station OBS5. High seismic velocities above the BSR and low seismic velocities below the BSR document the presence of gas hydrate and free gas, respectively, along the Vestnesa Ridge. We derive gas hydrate saturations from seismic velocity models using the SCA/DEM approach. Results suggest up to 10–18% average gas hydrate saturation and 1.5–4.1% average free gas saturation in layers near the BSR depth. We find high gas hydrate and free gas saturations near the ridge crest, except at few locations potentially shadowed by the fault where gas hydrate and free gas saturations are lower. Hence, we suggest structural and topographical control on the distribution of gas hydrates and free gas along the ridge. Gas hydrate saturations estimated in this study are different from gas hydrate saturations estimated using resistivity data. Gas hydrate-filled fracture deposits or coexistence of gas and gas hydrate in GHSZ can create such differences. Combined analysis from  $P$  and  $S$  wave velocity models, seismic  $Q$  model, and resistivity data suggest the coexistence of free gas and gas hydrates in the GHSZ northeast of the fault.



Appendix A

Ocean-bottom seismic (OBS) data are often used to derive subsurface *S* wave velocity model in marine settings using reflected converted wave (PS) signals recorded by horizontal components of the seismometer (Bünz et al., 2005; Dash & Spence, 2011; Exley et al., 2010; Satyavani et al., 2016; Westbrook et al., 2008). Converted waves travel downward as *P* waves and upon reflection are converted into *S* waves, hence the name PS-waves, or converted waves. A *P* wave velocity model is required to derive *S* wave velocities from PS reflections. The analysis of the *P* wave velocity model constrains the geometry of the subsurface model, that is, depths of interfaces. Thus, it is necessary to correlate picked reflection arrivals in a PP section with reflection arrivals in the corresponding PS section (Kumar et al., 2007; Westbrook et al., 2008). Seismic signatures in PP and PS sections recorded by OBS data are quite different (Figures 2 and 4) as reflectivity in a PS section depends on several parameters (Aki & Richards, 1980; Connolly, 1999; Duffaut et al., 2000) that are different from PP reflectivity. Reflections that are strong in a PP section, for example, strong reflections due to the presence of free gas, might not be strong in a PS section (Bünz et al., 2005). Resolution in a PS section is also higher as *S* wave velocities are lower than *P* wave velocities. This may result in a PS section that has continuous reflections from different reflectors in the subsurface (Figure A1a). All these factors, accompanied by low signal-to-noise ratio due to poor coupling between seafloor and seismometer in many cases, make it hard to match PP reflection arrivals with their corresponding PS reflection arrivals. Correlation of arrivals in these two sections is a major source of error in the derived *S* wave velocities (Westbrook et al., 2008).

In the present study, we have used a semblance approach in a layer stripping fashion to find corresponding reflections in the PP and PS sections. For example, in order to find a reflection arrival in a PS section

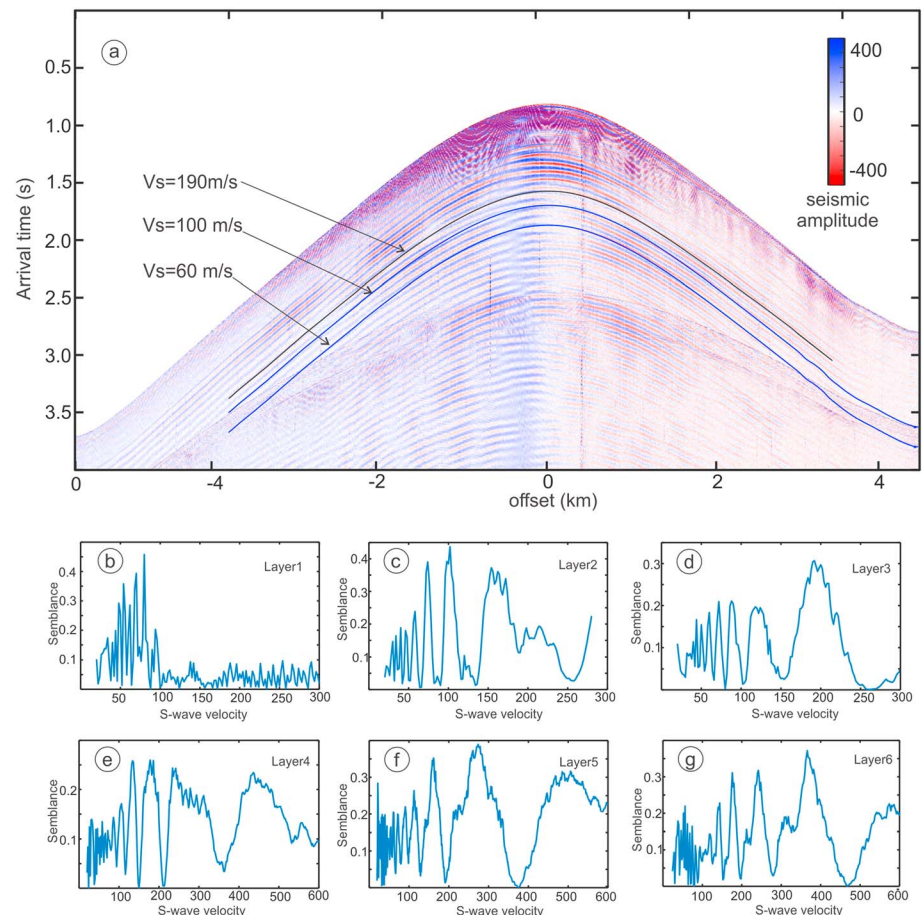


**Figure A1.** (a) *S* wave data recorded at site OBS5. Three travel curves show curvature for different possible *S* wave interval velocities in the Layer 3. (b–g) Semblance plot for different *S* wave interval velocities.

corresponding to the first picked reflection in a PP section, semblance is calculated for different  $S$  wave velocities in the first layer. Since parameters like  $P$  wave velocity and depth of a reflector are fixed in a  $P$  wave velocity model, different  $S$  wave velocities will result in different PS reflection arrivals.

$$S_{vs} = \frac{\left[ \sum_{j=1}^N A_j(t) \right]^2}{N \left[ \sum_{j=1}^N A_j(t)^2 \right]}$$

Here  $S_{vs}$  is the semblance for a given reflection arrival corresponding to a given  $v_s$  ( $S$  wave velocity).  $A_j(t)$  is the amplitude of  $j$ th sample along a reflection arrival corresponding to a given  $v_s$ .  $N$  is the total number of samples picked along a reflection arrival.

We expect maximum coherence for a PS reflection arrival corresponding to appropriate reflector in the PS section. Figures A1b–A1g show the semblance plot for different layers. We, therefore, pick and analyze PS reflection arrivals corresponding to  $S$  wave velocities that lie within the range of possible  $S$  wave velocity values and corresponds to strong semblance values in the semblance plot.

### Acknowledgments

This work is partly supported by the Research Council of Norway through its Centres of Excellence funding scheme, project 223259. We thank the crew of the  $R/V$  Helmer Hanssen and those who contributed to the OBS and  $P$ -cable data acquisition. We thank Andreia Plaza-Faverola, Kate Waghorn, and Sunil Vadakkepuliambatta for their help in this work. We also thank anonymous reviewers and Ingo Pecher (Associate Editor) for their careful reading of the work and constructive suggestions that improved the manuscript. The data are stored at UiT open research data repository (<https://doi.org/10.18710/EOIBYF>).

### References

- Aki, K., & Richards, P. G. (1980). *Quantitative seismology, theory and methods* (p. 557). San Francisco: W.H. Freeman and Co.
- Bhatnagar, G., Chapman, W. G., Dickens, G. R., Dugan, B., & Hirasaki, G. J. (2007). Generalization of gas hydrate distribution and saturation in marine sediments by scaling of thermodynamic and transport processes. *American Journal of Science*, 307(6), 861–900. <https://doi.org/10.2475/06.2007.01>
- Bickel, S. (1990). Velocity-depth ambiguity of reflection traveltimes. *Geophysics*, 55(3), 266–276. <https://doi.org/10.1190/1.1442834>
- Brooks, J. M., Cox, H. B., Bryant, W. R., Kennicutt, M. C. II, Mann, R. G., & McDonald, T. J. (1986). Association of gas hydrates and oil seepage in the Gulf of Mexico. *Organic Geochemistry*, 10(1-3), 221–234. [https://doi.org/10.1016/0146-6380\(86\)90025-2](https://doi.org/10.1016/0146-6380(86)90025-2)
- Brown, R. J., Stewart, R. R., & Lawton, D. C. (2002). A proposed polarity standard for multicomponent seismic data. *Geophysics*, 67(4), 1028–1037. <https://doi.org/10.1190/1.1500363>
- Bünz, S., Mienert, J., Vanneste, M., & Andreassen, K. (2005). Gas hydrates at the Storegga Slide: Constraints from an analysis of multi-component, wide-angle seismic data. *Geophysics*, 70(5), B19–B34. <https://doi.org/10.1190/1.2073887>
- Bünz, S., Polyanov, S., Vadakkepuliambatta, S., Consolaro, C., & Mienert, J. (2012). Active gas venting through hydrate-bearing sediments on the Vestnesa Ridge, offshore W-Svalbard. *Marine Geology*, 332–334, 189–197. <https://doi.org/10.1016/j.margeo.2012.09.012>
- Carcione, J. M., & Tinivella, U. (2000). Bottom-simulating reflectors: Seismic velocities and AVO effects. *Geophysics*, 65(1), 54–67. <https://doi.org/10.1190/1.1444725>
- Červený, V. (2001). *Seismic ray theory*. Cambridge: Cambridge University Press. <https://doi.org/10.1017/CBO9780511529399>
- Chand, S., Minshull, T. A., Davide, G., & Carcione, J. M. (2004). Elastic velocity models for gas-hydrate-bearing sediments—A comparison. *Geophysical Journal International*, 159(2), 573–590. <https://doi.org/10.1111/j.1365-246X.2004.02387.x>
- Chand, S., Minshull, T. A., Priest, J. F., Best, A. I., Clayton, C. R. I., & Waite, W. F. (2006). An effective medium inversion algorithm for gas hydrate quantification and its application to laboratory and borehole measurements of gas hydrate-bearing sediments. *Geophysical Journal International*, 166(2), 543–552. <https://doi.org/10.1111/j.1365-246X.2006.03038.x>
- Çiftçi, D., Al-Ali, M., & Verschuur, D. (2008). Assessing estimated velocity-depth models: Finding error bars in tomographic inversion. *Geophysics*, 73(5), VE223–VE233. <https://doi.org/10.1190/1.2951469>
- Collett, T. S., Boswell, R., Cochran, J. R., Kumar, P., Lall, M., Mazumdar, A., et al. (2014). Geologic implications of gas hydrates in the offshore of India: Results of the National Gas Hydrate Program Expedition 01. *Marine and Petroleum Geology*, 58, 3–28. <https://doi.org/10.1016/j.marpetgeo.2014.07.021>
- Collett, T. S., Lee, M. W., Zyrianova, M. V., Mrozewski, S. A., Guerin, G., Cook, A. E., & Goldberg, D. S. (2012). Gulf of Mexico Gas Hydrate Joint Industry Project Leg II logging-while-drilling data acquisition and analysis. *Marine and Petroleum Geology*, 34(1), 41–61. <https://doi.org/10.1016/j.marpetgeo.2011.08.003>
- Connolly, P. (1999). Elastic impedance. *The Leading Edge*, 18(4), 438–452. <https://doi.org/10.1190/1.1438307>
- Cook, A., Anderson, B. I., Malinverno, A., Mrozewski, S., & Goldberg, D. S. (2010). Electrical anisotropy due to gas hydrate-filled fractures. *Geophysics*, 75(6), F173–F185. <https://doi.org/10.1190/1.3506530>
- Cook, A. E., & Waite, W. F. (2018). Archie's saturation exponent for natural gas hydrate in coarse-grained reservoirs. *Journal of Geophysical Research: Solid Earth*, 123, 2069–2089. <https://doi.org/10.1002/2017jb015138>
- Daigle, H., & Dugan, B. (2011). Capillary controls on methane hydrate distribution and fracturing in advective systems. *Geochemistry, Geophysics, Geosystems*, 12, Q01003. <https://doi.org/10.1029/2010GC003392>
- Dash, R., & Spence, G. (2011). P-wave and S-wave velocity structure of northern Cascadia margin gas hydrates. *Geophysical Journal International*, 187(3), 1363–1377. <https://doi.org/10.1111/j.1365-246X.2011.05215.x>
- Davie, M. K., & Buffett, B. A. (2001). A numerical model for the formation of gas hydrate below the seafloor. *Journal of Geophysical Research*, 106(B1), 497–514. <https://doi.org/10.1029/2000JB900363>
- Davie, M. K., & Buffett, B. A. (2003). A steady state model for marine hydrate formation: Constraints on methane supply from pore water sulfate profiles. *Journal of Geophysical Research*, 108(B10), 2495. <https://doi.org/10.1029/2002JB002300>
- Delescluse, M., Nedimović, M. R., & Loudon, K. E. (2011). 2D waveform tomography applied to long-streamer MCS data from the Scotian Slope. *Geophysics*, 76(4), B151–B163. <https://doi.org/10.1190/1.3587219>
- Dix, C. (1955). Seismic velocities from surface measurements. *Geophysics*, 20(1), 68–86. <https://doi.org/10.1190/1.1438126>
- Duffaut, K., Alsos, T., Landro, M., & Rognoe, H. (2000). Shear-wave elastic impedance. *The Leading Edge*, 19(11), 1223–1229.
- Ecker, C., Dvorkin, J., & Nur, A. (1998). Sediments with gas hydrates: Internal structure from seismic AVO. *Geophysics*, 63(5), 1659–1669. <https://doi.org/10.1190/1.1444462>

- Ecker, C., Dvorkin, J., & Nur, A. (2000). Estimating the amount of gas hydrate and free gas from marine seismic data. *Geophysics*, *65*(2), 565–573. <https://doi.org/10.1190/1.1444752>
- Eiken, O., & Hinze, K. (1993). Contourites in the Fram Strait. *Sedimentary Geology*, *82*(1-4), 15–32. [https://doi.org/10.1016/0037-0738\(93\)90110-Q](https://doi.org/10.1016/0037-0738(93)90110-Q)
- Engen, Ø., Faleide, J. I., & Dyreng, T. K. (2008). Opening of the Fram Strait gateway: A review of plate tectonic constraints. *Tectonophysics*, *450*(1-4), 51–69. <https://doi.org/10.1016/j.tecto.2008.01.002>
- Exley, R. J. K., Westbrook, G. K., Haacke, R. R., & Peacock, S. (2010). Detection of seismic anisotropy using ocean bottom seismometers: A case study from the northern headwall of the Storegga Slide. *Geophysical Journal International*, *183*(1), 188–210. <https://doi.org/10.1111/j.1365-246X.2010.04730.x>
- Gaiser, J. E. (1999). Applications for vector coordinate systems of 3-D converted wave data. *The Leading Edge*, *18*(11), 1290–1300. <https://doi.org/10.1190/1.1438202>
- Ghosh, R., Sain, K., & Ojha, M. (2010). Effective medium modeling of gas hydrate-filled fractures using the sonic log in the Krishna-Godavari basin, offshore eastern India. *Journal of Geophysical Research*, *115*, B06101. <https://doi.org/10.1029/2009JB006711>
- Goswami, B. K., Weittemeyer, K. A., Minshull, T. A., Sinha, M. C., Westbrook, G. K., Chabert, A., & Ker, S. (2015). A joint electromagnetic and seismic study of an active pockmark within the hydrate stability field at the Vestnesa Ridge, West Svalbard margin. *Journal of Geophysical Research: Solid Earth*, *120*, 6797–6822. <https://doi.org/10.1002/2015JB012344>
- Hamilton, E. L. (1978). Sound velocity-density relations in sea-floor sediments and rocks. *The Journal of the Acoustical Society of America*, *63*(4), 366–377.
- Helgerud, M. B., Dvorkin, J., Nur, A., Sakai, A., & Collett, T. (1999). Effective wave velocity in marine sediments with gas hydrates: Effective medium modeling. *Geophysical Research Letters*, *26*(13), 2021–2024. <https://doi.org/10.1029/1999GL900421>
- Hobro, J. W., Minshull, T. A., & Singh, S. C. (1998). Tomographic seismic studies of the methane hydrate stability zone in the Cascadia Margin. *Geological Society, London, Special Publications*, *137*(1), 133–140. <https://doi.org/10.1144/gsl.sp.1998.137.01.10>
- Howe, J. A., Shimmield, T. M., & Harland, R. (2008). Late Quaternary contourites and glaciomarine sedimentation in the Fram Strait. *Sedimentology*, *55*, 179–200. <https://doi.org/10.1111/j.1365-3091.2007.00897.x>
- Hustoft, S., Bünz, S., Mienert, J., & Chand, S. (2009). Gas hydrate reservoir and active methane-venting province in sediments on <20 Ma young oceanic crust in the Fram Strait, offshore NW-Svalbard. *Earth and Planetary Science Letters*, *284*(1-2), 12–24. <https://doi.org/10.1016/j.epsl.2009.03.038>
- Hyndman, R. D., & Davis, E. E. (1992). A mechanism for the formation of methane hydrate and seafloor bottom simulating reflectors by vertical fluid expulsion. *Journal of Geophysical Research*, *97*(B5), 7025–7041. <https://doi.org/10.1029/91JB03061>
- Hyndman, R. D., & Spence, G. D. (1992). A seismic study of methane hydrate marine bottom simulating reflectors. *Journal of Geophysical Research*, *97*(B5), 6683–6698. <https://doi.org/10.1029/92JB00234>
- Jaiswal, P., Dewangan, P., Ramprasad, T., & Zelt, C. A. (2012). Seismic characterization of hydrates in faulted, fine-grained sediments of Krishna-Godavari Basin: Full waveform inversion. *Journal of Geophysical Research*, *117*, B10305. <https://doi.org/10.1029/2012JB009201>
- Jakobsen, M., Hudson, J. A., Minshull, T. A., & Singh, S. C. (2000). Elastic properties of hydrate-bearing sediments using effective medium theory. *Journal of Geophysical Research*, *105*(B1), 561–577. <https://doi.org/10.1029/1999JB900190>
- Julian, B. R., & Gubbins, D. (1977). Three-dimensional seismic ray tracing. *Journal of Geophysical Research*, *43*, 95–114.
- Katzman, R., Holbrook, W. S., & Paull, C. K. (1994). Combined vertical-incidence and wide-angle seismic study of a gas hydrate zone, Blake ridge. *Journal of Geophysical Research*, *99*(B9), 17,975–17,995. <https://doi.org/10.1029/94JB00662>
- Kemett, B. L. N., & Kerry, N. J. (1979). Seismic waves in a stratified half space. *Geophysical Journal of the Royal Astronomical Society*, *57*, 557–583.
- Kennedy, W. D., & Herrick, D. C. (2004). Conductivity anisotropy in shale-free sandstone. *Petrophysics*, *45*, 38–58.
- Kennedy, W. D., Herrick, D. C., & Yao, T. (2001). Calculating water saturation in electrically anisotropic media. *Petrophysics*, *42*, 118–136.
- Knies, J., Daszinnies, M., Plaza-Faverola, A., Chand, S., Sylta, Ø., Bünz, S., et al. (2018). Modelling persistent methane seepage offshore western Svalbard since early Pleistocene. *Marine and Petroleum Geology*, *91*, 800–811. <https://doi.org/10.1016/j.marpetgeo.2018.01.020>
- Knies, J., Matthiessen, J., Vogt, C., Laberg, J. S., Hjelstuen, B. O., Smelror, M., et al. (2009). The Plio-Pleistocene glaciation of the Barents Sea-Svalbard region: A new model based on revised chronostratigraphy. *Quaternary Science Reviews*, *28*(9-10), 812–829. <https://doi.org/10.1016/j.quascirev.2008.12.002>
- Korenaga, J., Holbrook, W. S., Singh, S. C., & Minshull, T. A. (1997). Natural gas hydrates on the southeast U.S. margin: Constraints from full waveform and travel time inversions of wide-angle seismic data. *Journal of Geophysical Research*, *102*(B7), 15,345–15,365. <https://doi.org/10.1029/97JB00725>
- Kumar, D., Sen, M. K., & Bangs, N. L. (2007). Gas hydrate concentration and characteristics within Hydrate Ridge inferred from multi-component seismic reflection data. *Journal of Geophysical Research*, *112*, B12306. <https://doi.org/10.1029/2007JB004993>
- Kvenvolden, K. A., & Barnard, L. A. (1983). Hydrates of natural gas in continental margins. *Studies in Continental Margin Geology*, *34*, 631–640.
- Lee, M. W., & Collett, T. S. (2009). Gas hydrate saturations estimated from fractured reservoir at Site NGHP-01-10, Krishna-Godavari Basin, India. *Journal of Geophysical Research*, *114*, B07102. <https://doi.org/10.1029/2008JB006237>
- Lee, M. W., & Collett, T. S. (2012). Pore- and fracture-filling gas hydrate reservoirs in the Gulf of Mexico Gas Hydrate Joint Industry Project Leg II Green Canyon 955 H well. *Marine and Petroleum Geology*, *34*(1), 62–71. <https://doi.org/10.1016/j.marpetgeo.2011.08.002>
- Lee, M. W., Hutchinson, D. R., Collett, T. S., & Dillon, W. P. (1996). Seismic velocities for hydrate-bearing sediments using weighted equation. *Journal of Geophysical Research*, *101*(B9), 20,347–20,358. <https://doi.org/10.1029/96JB01886>
- Lines, L. (1993). Ambiguity in analysis of velocity and depth. *Geophysics*, *58*(4), 596–597. <https://doi.org/10.1190/1.1443443>
- Liu, X., & Flemings, P. B. (2007). Dynamic multiphase flow model of hydrate formation in marine sediments. *Journal of Geophysical Research*, *112*, B03101. <https://doi.org/10.1029/2005JB004227>
- Liu, X., & Flemings, P. B. (2011). Capillary effects on hydrate stability in marine sediments. *Journal of Geophysical Research*, *116*, B07102. <https://doi.org/10.1029/2010JB008143>
- Lu, S., & McMechan, G. A. (2002). Estimation of gas hydrate and free gas saturation, concentration, and distribution from seismic data. *Geophysics*, *67*(2), 582–593. <https://doi.org/10.1190/1.1468619>
- Marín-Moreno, H., Sahoo, S. K., & Best, A. I. (2017). Theoretical modeling insights into elastic wave attenuation mechanisms in marine sediments with pore-filling methane hydrate. *Journal of Geophysical Research: Solid Earth*, *122*, 1835–1847. <https://doi.org/10.1002/2016JB013577>
- McKenzie, D. A. N., & O’Nions, R. K. (1991). Partial melt distributions from inversion of rare earth element concentrations. *Journal of Petrology*, *32*(5), 1021–1091. <https://doi.org/10.1093/ptrology/32.5.1021>



- Minshull, T., & White, R. (1989). Sediment compaction and fluid migration in the Makran accretionary prism. *Journal of Geophysical Research*, 94(B6), 7387–7402. <https://doi.org/10.1029/JB094iB06p07387>
- Minshull, T. A., & Chand, S. (2009). The pore-scale distribution of sediment-hosted hydrates: Evidence from effective medium modelling of laboratory and borehole seismic data. *Geological Society, London, Special Publications*, 319(1), 93–101. <https://doi.org/10.1144/SP319.8>
- Minshull, T. A., & Singh, S. C. (1993). Shallow structure of oceanic crust in the western North Atlantic from seismic waveform. *Journal of Geophysical Research*, 98(B2), 1777–1792. <https://doi.org/10.1029/92JB02136>
- Minshull, T. A., Singh, S. C., & Westbrook, G. K. (1994). Seismic velocity structure at a gas hydrate reflector, offshore western Colombia from full waveform inversion. *Journal of Geophysical Research*, 99(B3), 4715–4734. <https://doi.org/10.1029/93JB03282>
- Nakanishi, N., & Yamaguchi, K. (1986). A numerical experiment on nonlinear image reconstruction from first-arrival times for two-dimensional island arc structure. *Journal of Physics of the Earth*, 34(2), 195–201. <https://doi.org/10.4294/jpe1952.34.195>
- Nishizawa, O. (1982). Seismic velocity anisotropy in a medium containing oriented cracks: Transversely isotropic case. *Journal of Physics of the Earth*, 30(4), 331–347. <https://doi.org/10.4294/jpe1952.30.331>
- Nole, M., Daigle, H., Cook, A. E., Malinverno, A., & Flemings, P. B. (2018). Burial-driven methane recycling in marine gas hydrate systems. *Earth and Planetary Science Letters*, 499, 197–204. <https://doi.org/10.1016/j.epsl.2018.07.036>
- Ottesen, D., Dowdeswell, J. A., & Rise, L. (2005). Submarine landforms and the reconstruction of fast-flowing ice streams within a large Quaternary ice sheet: The 2500-km-long Norwegian-Svalbard margin (57–80 N). *Geological Society of America Bulletin*, 117(7), 1033–1050. <https://doi.org/10.1130/B25577.1>
- Panieri, G., Bünz, S., Fornari, D. J., Escartin, J., Serov, P., Jansson, P., et al. (2017). An integrated view of the methane system in the pockmarks at Vestnesa Ridge, 79°N. *Marine Geology*, 390, 282–300. <https://doi.org/10.1016/j.margeo.2017.06.006>
- Pecher, I. A., Minshull, T. A., Singh, S. C., & Huene, R. V. (1996). Velocity structure of a bottom simulating reflector offshore Peru: Results from full waveform inversion. *Earth and Planetary Science Letters*, 139(3–4), 459–469. [https://doi.org/10.1016/0012-821X\(95\)00242-5](https://doi.org/10.1016/0012-821X(95)00242-5)
- Petersen, C. J., Bunz, S., Huston, S., Mienert, J., & Klaeschen, D. (2010). High-resolution P-Cable 3D seismic imaging of gas chimney structures in gas hydrated sediments of an Arctic sediment drift. *Marine and Petroleum Geology*, 27(9), 1981–1994. <https://doi.org/10.1016/j.marpetgeo.2010.06.006>
- Planke, S., Eriksen, F. N., Berndt, C., Mienert, J., & Masson, D. (2009). Spotlight on technology: P-cable high-resolution seismic. *Oceanography*, 22(1), 85. <https://doi.org/10.5670/oceanog.2009.09>
- Plaza-Faverola, A., Bünz, S., Johnson, J. E., Chand, S., Knies, J., Mienert, J., & Franek, P. (2015). Role of tectonic stress in seepage evolution along the gas hydrate-charged Vestnesa Ridge, Fram Strait. *Geophysical Research Letters*, 42, 733–742. <https://doi.org/10.1002/2014GL062474>
- Plaza-Faverola, A., Bünz, S., & Mienert, J. (2010). Fluid distributions inferred from P-wave velocity and reflection seismic amplitude anomalies beneath the Nyegga pockmark field of the mid-Norwegian margin. *Marine and Petroleum Geology*, 27(1), 46–60. <https://doi.org/10.1016/j.marpetgeo.2009.07.007>
- Posewang, J., & Mienert, J. (1999). The enigma of double BSRs: Indicators for changes in the hydrate stability field. *Geo-Marine Letters*, 19(1–2), 157–163. <https://doi.org/10.1007/s003670050103>
- Qin, F., Luo, Y., Olsen, K., Cai, W., & Schuster, G. (1992). Finite-difference solution of the eikonal equation along expanding wavefronts. *Geophysics*, 57(3), 478–487. <https://doi.org/10.1190/1.1443263>
- Rawlinson, N., Hauser, J., & Sambridge, M. (1998). Seismic ray tracing and wavefront tracking in laterally heterogeneous media. *Advances in Geophysics*, 49(1), 203–273. [https://doi.org/10.1016/S0065-2687\(07\)49003-3](https://doi.org/10.1016/S0065-2687(07)49003-3)
- Rawlinson, N., & Sambridge, M. (2004). Wave front evolution in strongly heterogeneous layered media using the fast marching method. *Geophysical Journal International*, 156(3), 631–647. <https://doi.org/10.1111/j.1365-246X.2004.02153.x>
- Rempel, A. W. (2011). A model for the diffusive growth of hydrate saturation anomalies in layered sediments. *Journal of Geophysical Research*, 116, B10105. <https://doi.org/10.1029/2011JB008484>
- Rempel, A. W., & Buffett, B. A. (1997). Formation and accumulation of gas hydrate in porous media. *Journal of Geophysical Research*, 102(B5), 10,151–10,164. <https://doi.org/10.1029/97JB00392>
- Richardson, M. D., Muzi, E., Miaschi, B., & Turgutcan, F. (1991). Shear wave velocity gradients in near-surface marine sediments. In J. M. Hovem, M. Richardson, & R. D. Stoll (Eds.), *Shear Waves in Marine Sediments* (pp. 295–304). Dordrecht: Kluwer Academic Publishers.
- Ritzmann, O., Jokat, W., Czuba, W., Guterch, A., Mjelde, R., & Nishimura, Y. (2004). A deep seismic transect from Hovgård Ridge to northwestern Svalbard across the continental-ocean transition: A sheared margin study. *Geophysical Journal International*, 157(2), 683–702. <https://doi.org/10.1111/j.1365-246X.2004.02204.x>
- Sahoo, S. K., Marin-Moreno, H., North, L. J., Falcon-Suarez, I., Madhusudhan, B. N., Best, A. I., & Minshull, T. A. (2018). Presence and consequences of coexisting methane gas with hydrate under two phase water-hydrate stability conditions. *Journal of Geophysical Research: Solid Earth*, 123, 3377–3390. <https://doi.org/10.1029/2018JB015598>
- Satyavani, N., Sain, K., & Gupta, H. (2016). Ocean bottom seismometer data modeling to infer gas hydrate saturation in Krishna-Godavari (KG) basin. *Journal of Natural Gas Science and Engineering*, 33, 908–917. <https://doi.org/10.1016/j.jngse.2016.06.037>
- Sheng, P. (1990). Effective-medium theory of sedimentary rocks. *Physics Reviews B*, 41(7), 4507–4512. <https://doi.org/10.1103/PhysRevB.41.4507>
- Sheriff, R. E., & Geldart, L. P. (1982). *Exploration seismology* (Vol. I p. 106). Cambridge: Cambridge University Press.
- Shinohara, M., Hirata, N., & Takahashi, N. (1994). High resolution velocity analysis of ocean bottom seismometer data by the τ-p method. *Marine Geophysical Researches*, 16(3), 185–199. <https://doi.org/10.1007/BF01237513>
- Shipley, T. H., Houston, M. H., Buffler, R. T., Shaub, F. J., McMillen, K. J., Ladd, J. W., & Worzel, J. L. (1979). Seismic evidence for widespread possible gas hydrate horizons on continental slopes and rises. *AAPG Bulletin*, 63, 2204–2213.
- Singh, S. C., Minshull, T. A., & Spence, G. D. (1993). Velocity structure of a gas hydrate reflector. *Science*, 260(5105), 204–207. <https://doi.org/10.1126/science.260.5105.204>
- Singhroha, S., Bünz, S., Plaza-Faverola, A., & Chand, S. (2016). Gas hydrate and free gas detection using seismic quality factor estimates from high-resolution P-cable 3D seismic data. *Interpretation (Tulsa)*, 4(1), SA39–SA54. <https://doi.org/10.1190/INT-2015-0023.1>
- Sloan, E. D. Jr. (1998). *Clathrate hydrates of natural gases* (2nd ed.). New York: Marcel Dekker Inc.
- Smith, A. J., Mienert, J., Bünz, S., & Greinert, J. (2014). Thermogenic methane injection via bubble transport into the upper Arctic Ocean from the hydrate-charged Vestnesa Ridge, Svalbard. *Geochemistry, Geophysics, Geosystems*, 15, 1945–1959. <https://doi.org/10.1002/2013GC005179>
- Song, J. L., & ten Brink, U. (2004). RayGUI 2.0—A graphical user interface for interactive forward and inversion ray-tracing, U.S. Geological Survey Open-File Report 2004-1426.

- Song, S., Tinivella, U., Giustiniani, M., Singhroha, S., Büinz, S., & Cassiani, G. (2018). OBS data analysis to quantify gas hydrate and free gas in the South Shetland Margin (Antarctica). *Energies*, *11*(12), 3290. <https://doi.org/10.3390/en11123290>
- Spence, G. D., Minshull, T. A., & Fink, C. (1995). Seismic studies of methane gas hydrate, offshore Vancouver Island. In *Proceedings-Ocean Drilling Program Scientific Results* (Vol. 146 (part 1), pp. 163–174). Texas A&M University. <https://doi.org/10.2973/odp.proc.sr.146-1.1995>
- Stoll, R. D., Ewing, J. I., & Bryan, G. M. (1971). Anomalous wave velocities in sediments containing gas hydrates. *Journal of Geophysical Research*, *76*(8), 2090–2094. <https://doi.org/10.1029/JB076i008p02090>
- Stranne, C., O'Regan, M., & Jakobsson, M. (2017). Modeling fracture propagation and seafloor gas release during seafloor warming-induced hydrate dissociation. *Geophysical Research Letters*, *44*, 8510–8519. <https://doi.org/10.1002/2017GL074349>
- Thomsen, L. (1986). Weak elastic anisotropy. *Geophysics*, *51*(10), 1954–1966. <https://doi.org/10.1190/1.1442051>
- Thomsen, L. (1999). Converted-wave reflection seismology over inhomogeneous, anisotropic media. *Geophysics*, *64*(3), 678–690. <https://doi.org/10.1190/1.1444577>
- Tréhu, A. M., Long, P. E., Torres, M. E., Bohrmann, G., Rack, F. R., Collett, T. S., et al. (2004). Three-dimensional distribution of gas hydrate beneath southern Hydrate Ridge: Constraints from ODP Leg 204. *Earth and Planetary Science Letters*, *222*(3-4), 845–862. <https://doi.org/10.1016/j.epsl.2004.03.035>
- Vidale, J. (1988). Finite-difference calculation of travel times. *Bulletin of the Seismological Society of America*, *78*(6), 2062–2076.
- Virieux, J., & Farra, V. (1991). Ray tracing in 3-D complex isotropic media: An analysis of the problem. *Geophysics*, *56*(12), 2057–2069. <https://doi.org/10.1190/1.1443018>
- Vogt, P. R., Crane, K., Sundvor, E., Max, M. D., & Pfirman, S. L. (1994). Methane-generated (?) pockmarks on young, thickly sedimented oceanic crust in the Arctic: Vestnesa Ridge, Fram Strait. *Geology*, *22*(3), 255–258. [https://doi.org/10.1130/0091-7613\(1994\)022<0255:MGPOYT>2.3.CO;2](https://doi.org/10.1130/0091-7613(1994)022<0255:MGPOYT>2.3.CO;2)
- Wang, J., Jaiswal, P., Haines, S. S., Hart, P. E., & Wu, S. (2018). Gas hydrate quantification using full-waveform inversion of sparse ocean-bottom seismic data: A case study from Green Canyon Block 955, Gulf of Mexico. *Geophysics*, *83*(4), B167–B181. <https://doi.org/10.1190/geo2017-0414.1>
- Wang, Y., & Houseman, G. A. (1995). Tomographic inversion of reflection seismic amplitude data for velocity variation. *Geophysical Journal International*, *123*(2), 355–372. <https://doi.org/10.1111/j.1365-246X.1995.tb06859.x>
- Weitemeyer, K. A., Constable, S., & Tréhu, A. M. (2011). A marine electromagnetic survey to detect gas hydrate at Hydrate Ridge, Oregon. *Geophysical Journal International*, *187*(1), 45–62. <https://doi.org/10.1111/j.1365-246X.2011.05105.x>
- Westbrook, G. K., Carson, B., Musgrave, R. J., Ashi, J., Baranow, B., Brown, K. M., et al. (1994). *Proceedings of the Ocean Drilling Program, Initial Reports* (Vol. 146 (Pt. 1)). College Station, TX: Ocean Drilling Program.
- Westbrook, G. K., Chand, S., Rossi, G., Long, C., Büinz, S., Camerlenghi, A., et al. (2008). Estimation of gas hydrate concentration from multi-component seismic data at sites on the continental margins of NW Svalbard and the Storegga region of Norway. *Marine and Petroleum Geology*, *25*(8), 744–758. <https://doi.org/10.1016/j.marpetgeo.2008.02.003>
- Willis, J. R. (1977). Bounds and self-consistent estimates for the overall properties of anisotropic composites. *Journal of the Mechanics and Physics of Solids*, *25*(3), 185–202. [https://doi.org/10.1016/0022-5096\(77\)90022-9](https://doi.org/10.1016/0022-5096(77)90022-9)
- Wood, A. B. (1941). *A textbook of sound*. New York: Macmillan.
- Wyllie, M. R., Gregory, A. R., & Gardner, G. H. P. (1958). An experimental investigations of factors affecting elastic wave velocities in porous media. *Geophysics*, *23*(3), 459–493. <https://doi.org/10.1190/1.1438493>
- Xia, G., Sen, M. K., & Stoffa, P. L. (1998). 1-D elastic waveform inversion: A divide-and-conquer approach. *Geophysics*, *63*(5), 1670–1684. <https://doi.org/10.1190/1.1444463>
- Xu, W., & Ruppel, C. (1999). Predicting the occurrence, distribution, and evolution of methane gas hydrate in porous marine sediments. *Journal of Geophysical Research*, *104*(B3), 5081–5095. <https://doi.org/10.1029/1998JB900092>
- Yilmaz, Ö. (2001). Seismic data analysis: Society of exploration geophysicists. <https://doi.org/10.1190/1.9781560801580>
- Yuan, T., Hyndman, R. D., Spence, G. D., & Desmons, B. (1996). Seismic velocity increase and deep-sea gas hydrate concentration above a bottom simulating reflector on the northern Cascadia continental slope. *Journal of Geophysical Research*, *101*(B6), 13,655–13,671. <https://doi.org/10.1029/96JB00102>
- Zelt, C. A., & Smith, R. B. (1992). Seismic travel-time inversion for 2-D crustal velocity structure. *Geophysical Journal International*, *108*(1), 16–34. <https://doi.org/10.1111/j.1365-246X.1992.tb00836.x>
- Zillmer, M., Flueh, E. R., & Petersen, J. (2005). Seismic investigation of a bottom simulating reflector and quantification of gas hydrate in the Black Sea. *Geophysical Journal International*, *161*(3), 662–678. <https://doi.org/10.1111/j.1365-246X.2005.02635.x>